

## HI SPECTROSCOPY OF REVERBERATION-MAPPED ACTIVE GALACTIC NUCLEI

JUSTIN H. ROBINSON<sup>1</sup>, MISTY C. BENTZ<sup>1</sup>, MEGAN C. JOHNSON<sup>2</sup>, HÉLÈNE M. COURTOIS<sup>3</sup>, AND BENJAMIN OU-YANG<sup>1</sup>

<sup>1</sup>Department of Physics and Astronomy, Georgia State University, Atlanta, GA 30303, USA; [jrob@astro.gsu.edu](mailto:jrob@astro.gsu.edu)

<sup>2</sup>United States Naval Observatory (USNO) 3450 Massachusetts Ave NW, Washington, DC 20392, USA and

<sup>3</sup>University of Lyon; UCB Lyon 1/CNRS/IN2P3; IPN Lyon, France

(Received; Accepted)  
Draft version June 18, 2019

### ABSTRACT

We present HI 21 cm spectroscopy from the GBT for the host galaxies of 31 nearby AGNs with direct  $M_{\text{BH}}$  measurements from reverberation mapping. These are the first published HI detections for 12 galaxies, and the spectral quality is generally an improvement over archival data for the remainder of the sample. We present measurements of emission-line fluxes, velocity widths, and recessional velocities from which we derive HI mass, total gas mass, and redshifts. Combining  $M_{\text{GAS}}$  with constraints on  $M_{\text{STARS}}$  allows exploration of the baryonic content of these galaxies. We find a typical  $M_{\text{GAS}}/M_{\text{STARS}}$  fraction of 10%, with a few reaching  $\sim 30$ –50%. We also examined several relationships between  $M_{\text{STARS}}$ ,  $M_{\text{GAS}}$ ,  $M_{\text{BH}}$ , baryonic mass, and morphological type. We find a weak preference for galaxies with larger  $M_{\text{GAS}}$  to host more massive black holes. We also find gas-to-stellar fractions to weakly correlate with later types in unbarred spirals, with an approximately constant fraction for barred spirals. Consistent with previous studies, we find declining  $M_{\text{GAS}}/M_{\text{STARS}}$  with increasing  $M_{\text{STARS}}$ , with a slope suggesting the gas reservoirs have been replenished. Finally, we find a clear relationship for  $M_{\text{BH}}-M_{\text{BARY}}$  with a similar slope as  $M_{\text{BH}}-M_{\text{STARS}}$  reported by [Bentz & Manne-Nicholas \(2018\)](#). The dwarf Seyfert NGC 4395 appears to follow this relationship as well, even though it has a significantly higher gas fraction and smaller  $M_{\text{BH}}$  than the remainder of our sample.

*Keywords:* galaxies: active – galaxies: nuclei – galaxies: Seyfert – radio lines: galaxies

### 1. INTRODUCTION

Hydrogen is the most abundant element in the universe ([Payne 1925](#)), and is of fundamental importance in galactic and extragalactic studies. The spin-flip transition of electrons in neutral hydrogen (HI) atoms gives rise to the hyperfine 21 cm line radiation, which is easily detected from gas-rich galaxies (usually late-type galaxies, e.g. [Haynes & Giovanelli 1984](#), and references therein).

The HI emission line provides a number of interesting details about the host galaxy. First, the Doppler-shifted recessional velocity yields one of the most reliable redshift measurements of extragalactic sources. Since the neutral gas is spread throughout the galaxy, it follows that the center velocity of the emission profile acts as a systemic velocity indicator. HI 21 cm emitting gas is also cold ( $\sim 120$  K), and reflects the overall motion of the disk as opposed to gas at hotter temperatures ( $\sim 10,000$  K) emitting in the optical (e.g. [O III]; [Osterbrock & Pogge 1987](#)). These higher temperature emission lines can be affected by the internal motion of the regions in which they emit, thus affecting the radial velocity and hence the redshift measurement (e.g., nuclear, optical emission lines reflecting net outflow motion; [Mirabel & Wilson 1984](#)).

Secondly, for inclined disk galaxies, the HI line width provides insight into their rotation speeds. The integrated emission profile is based on the distribution of radial velocities of the rotating disk, and correction for the disk’s inclination provides a constraint on the maximum rotation rate ([Fisher & Tully 1977](#)). Inclination-corrected widths of observed HI profiles are thus related to the rotation curves of disk galaxies ([Roberts 1969](#); [Epstein 1964](#)).

Finally, the total area under the integrated HI line provides an estimate of the total atomic gas content. For galaxies with angular extents smaller than the beam size of the telescope, the integrated HI flux is related to the total number of hy-

drogen atoms, and thus the mass in atomic hydrogen ( $M_{\text{HI}}$ ; [Roberts 1962](#)). Atomic hydrogen is normally the dominant gas phase in disk galaxies, with molecular hydrogen ( $\text{H}_2$ ) as the next significant component. HI has been observed to saturate and condense to  $\text{H}_2$  above a threshold surface density of  $\sim 10 M_{\odot} \text{pc}^{-2}$  ([Martin & Kennicutt 2001](#); [Wong & Blitz 2002](#); [Bigiel et al. 2008](#)), and giant molecular clouds are the dominant locations for star formation in spiral galaxies (e.g., [Leroy et al. 2008](#)). There have been many studies aimed at estimating the molecular gas content of disk galaxies (e.g., [Cortese et al. 2017](#)), for example showing that  $M_{\text{H}_2}/M_{\text{HI}}$  scales as a function of morphology ([Young & Knezek 1989](#); [McGaugh & de Blok 1997](#)). There is significant scatter in all of the distributions from [Young & Knezek \(1989\)](#), but the mean of their result for late-type spirals is  $M_{\text{H}_2}/M_{\text{HI}} \sim 0.2 \pm 0.1$ . Constraints on the solar helium abundance, the next most abundant element and significant gas mass contributor, place the  $M_{\text{He}}/M_{\text{HI}}$  fraction in the range of  $0.274 \pm 6\%$  ([Cox 2000](#)). The typical cosmic abundances of other elements such as carbon, nitrogen, and oxygen are only small fractions of the hydrogen abundance in spiral galaxies, including the Milky Way (e.g., [Spitzer 1998](#); [Obreschkow & Rawlings 2009](#)). Yet, the mass contribution from non-HI gas is typically less than the uncertainty involved in constraining  $M_{\text{HI}}$ . So the total gas mass of a galaxy ( $M_{\text{GAS}}$ ) is often estimated by simply applying a scale factor to  $M_{\text{HI}}$  to account for these contributions, the vast majority of which is helium ([McGaugh 2012](#), and references therein).

The first significant HI study of galaxies hosting an active galactic nucleus (AGN) was an exploration of the relationship between the disk and the nucleus of Seyfert galaxies by [Heckman et al. \(1978\)](#). That initial study hinted that the host galaxies of AGNs have a relationship between UV excess outside of the nucleus and the ratio of atomic gas to

galaxy luminosity ( $M_{\text{HI}}/L$ ; luminosities from Heckman et al. 1978 are derived from the B-band magnitudes from de Vaucouleurs et al. 1976), perhaps implying that feedback from nuclear activity triggers star formation in the larger galaxy disk. Heckman et al. (1978) also mention the tendency for Seyferts in their study with peculiar HI properties (e.g., HI absorption, abnormal  $M_{\text{HI}}/L$ ) to have peculiar morphological characteristics (e.g., double nucleus, one spiral arm, faint disk). Peck & Taylor (1998) conducted an HI kinematic study near the active core of NGC 3984, finding that all the HI components were redshifted with respect to the stellar content of the galaxy, which they interpreted as the signature of central parsec-scale gas infalling and feeding the nucleus. Fabello et al. (2011) used the Arecibo<sup>1</sup> Legacy Fast ALFA (ALFALFA) Survey (Giovanelli et al. 2005) to search for trends in the fraction of  $M_{\text{HI}}$  to stellar mass ( $M_{\text{STARS}}$ ) and black hole accretion rate. For galaxies with low star formation rates ( $\log \text{SFR}/M_{\text{STARS}} < -11.0$ ), the accretion rate scaled with increasing  $M_{\text{HI}}/M_{\text{STARS}}$ .

Not all of the literature points to correlations between HI content and AGN activity, though. For galaxies with moderate star formation rates ( $\log \text{SFR}/M_{\text{STARS}} > -11.0$ ) in the study by Fabello et al. (2011), no relationship was found between  $M_{\text{HI}}/M_{\text{STARS}}$  and accretion rate. Biegging & Biermann (1983) conducted HI studies of active and interacting galaxies and compared their HI fluxes to the Rieke (1978) survey of 10.6  $\mu\text{m}$  emission from Seyfert nuclei and found no correlation. Their reasoning was that the infrared fluxes refer only to the nucleus as opposed to the HI flux which originates from the entire disk, therefore concluding no connection between gas and AGN luminosity. Finally, in their review of coevolution of black holes in AGNs and properties of their hosts, Heckman & Best (2014) conclude from a number of studies that HI is unlikely to reside within the central regions of AGN host galaxies. Heckman & Best (2014) also mention that HI surface density in all spiral galaxies, whether active or inactive, is usually lower or near zero at the center, and gas present near the central supermassive black hole (SMBH) is likely to be primarily molecular in the case of inactive galaxies, or ionized in the case of AGN. Thus, there seems to be no clear picture of how the overall gas content of a galaxy is related to AGN fueling.

However, we know that active galaxies have gas accreting onto their central SMBHs, and that the gas reservoir is large enough and/or replenished often enough to fuel the black hole for  $\sim 10^7$  years (Martini 2004), perhaps multiple times in the history of the galaxy. The growth of the SMBHs in AGNs via accretion also appears to be related to the growth of the bulges of their host galaxies (see reviews by Heckman & Best 2014 and Kormendy & Ho 2013). The gas flows that fuel the accretion and growth of the SMBHs and bulges can be driven by mergers, with slower, gradual processes such as gravitational interactions with bar and spiral structures (Kormendy & Kennicutt 2004; Athanassoula 2008), or rapid, gas-rich disk instabilities (Genzel et al. 2014; Bournaud et al. 2010; Elmegreen et al. 2008; Dekel et al. 2009). Furthermore, over the past two decades it has become clear that galaxies and SMBHs have a symbiotic relationship, even though their typical size scales are different by orders of magnitude. Empirical scaling relationships between the central SMBH mass ( $M_{\text{BH}}$ ) and the host

galaxy itself have been the subjects of many studies (e.g., Ferrarese & Merritt 2000; Gebhardt et al. 2000; Kormendy & Ho 2013). It is therefore of interest to examine whether there is any relationship between  $M_{\text{BH}}$  and the gas properties of their host galaxies.

In this paper, we present the results of HI spectroscopy of 44 AGNs with direct  $M_{\text{BH}}$  measurements from the reverberation mapping database<sup>2</sup> of Bentz & Katz (2015). In Section 2, for those galaxies where HI emission is detected, we provide measurements of profile widths, recession velocities and thus redshifts, and HI flux. In Section 3, we detail our derived quantities of  $M_{\text{HI}}$  and  $M_{\text{GAS}}$  from the raw measurements, as well as other characteristics of the host galaxies and central black holes. In Section 4, we explore the relationship between  $M_{\text{BH}}$  and  $M_{\text{GAS}}$ , and we test relationships between  $M_{\text{BH}}$  and baryonic mass ( $M_{\text{BARY}}$ ), and  $M_{\text{GAS}}$  and  $M_{\text{STARS}}$ .

Throughout this work we adopt a  $\Lambda$ CDM cosmology of  $H_0 = 72 \text{ km s}^{-1} \text{ Mpc}^{-1}$  (Freedman et al. 2001),  $\Omega_{\text{M}}=0.3$ , and  $\Omega_{\Lambda}=0.7$  (Bennett et al. 2014).

## 2. DATA

### 2.1. Target Selection and Observations

Our ultimate goal for these observations is to employ the Tully-Fisher distance measurement method (Tully & Fisher 1977) to provide a significant number of distances for galaxies in the reverberation mapping sample. In this paper, however, we focus on the HI properties of the galaxies. We began with the database of all broad-lined AGNs with black hole masses derived from reverberation mapping (Bentz & Katz 2015). Because the Tully-Fisher method requires spiral galaxies, the AGNs hosted by elliptical galaxies were removed from the sample. Potential targets were then removed if they were at  $z > 0.1$ , and therefore likely outside the reach of the Tully-Fisher method (Reyes et al. 2011). Finally, the large, unblocked 100 m dish of the Robert C. Byrd Green Bank Telescope<sup>3</sup> (GBT) and its access to a large fraction of the sky make it ideal for sensitive 21 cm observations, therefore any remaining sources that were outside the pointing limits of the GBT were removed from the sample. The final selection consisted of 27 active galaxies observed in the spring of 2013 (project ID GBT13A-468; PI: Ou-Yang) and 17 active galaxies observed in the fall/winter of 2018-2019 (project ID GBT18B-258; PI: Robinson).

The GBT Spectrometer backend was used for GBT13A-468 and employed a 12.5 MHz bandwidth and 8,192 channels with velocity resolution of  $0.3 \text{ km s}^{-1} \text{ channel}^{-1}$ . The GBT Spectrometer has since been retired, so we employed the VERSatile GBT Astronomical Spectrometer (VEGAS) for GBT18B-258. The VEGAS mode we employed has an 11.72 MHz bandwidth, 32,768 channels, and velocity resolution of  $0.08 \text{ km s}^{-1} \text{ channel}^{-1}$ . The large 9'1 GBT L-Band beamwidth, defined as the full-width at half-maximum of the beam, encompassed even the largest optical angular sizes of our target galaxies.

Targets were observed in position-switched mode in pairs of equal on-off exposures, which were typically 60 second scans for GBT13A-468 and 120 second scans for GBT18B-258. All of the scans were divided into individual integrations of 3 seconds, so that if radio frequency interference (RFI) appeared, we could discard only the affected integrations rather

<sup>1</sup> The Arecibo Observatory is part of the National Astronomy and Ionosphere Center, which is operated by Cornell University under a cooperative agreement with the National Science Foundation.

<sup>2</sup> <http://www.astro.gsu.edu/AGNmass/>

<sup>3</sup> The Green Bank Observatory is a facility of the National Science Foundation operated under cooperative agreement by Associated Universities, Inc.

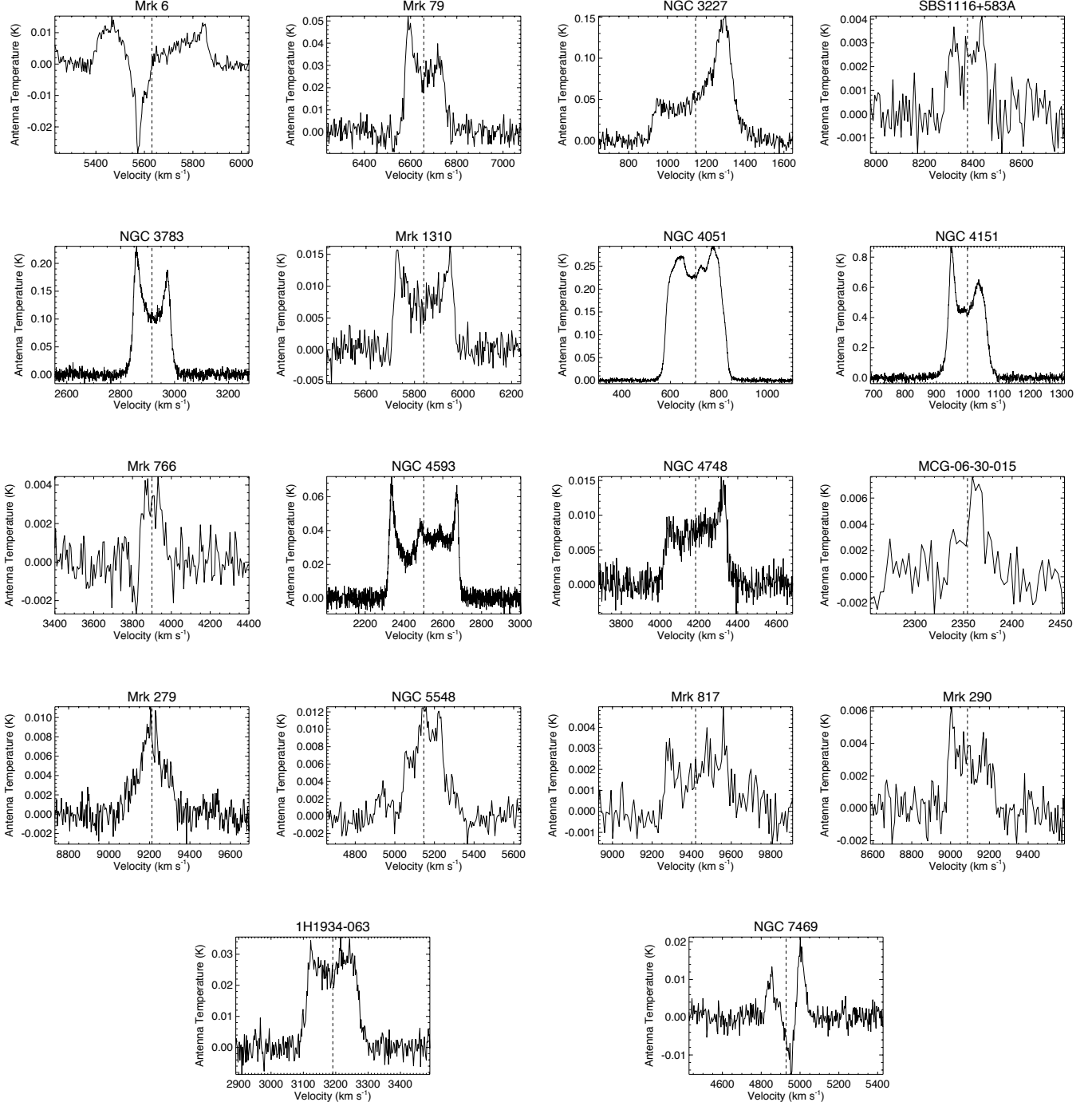


**Figure 1.** HI emission line spectra from GBT13A-468 after reduction, baseline subtraction, and smoothing with GBTIDL v2.8. Hanning smoothing was applied to all profiles, and further smoothing was dependent on the S/N (see Sec. 2.2). Note that Mrk 6 and NGC 7469 exhibit central absorption features. The vertical dashed lines indicate  $V_R$  measurements from `gmeasure`.

than the whole scan. Off-source sky observations allowed for the removal of the frequency structure of the raw band-pass and an improvement in the signal-to-noise ratio (S/N). Total on-source exposure times were estimated from the expected gas content of the galaxy (based on its morphological type), its expected distance (based on redshift), and a goal of achieving  $S/N=10$  in the peak flux of the HI emission line. We capped our initial time requests at 9 hours per source, but for a few weak yet promising targets, we requested and re-

ceived additional time to improve the S/N. In total, our observations covered 184 hours for GBT13A-468 and 208.25 hours for GBT18B-258, with total on-source exposure times ranging from  $\sim 6$  minutes to 16 hours. Table 1 lists the targets and the details of their observations.

## 2.2. Reduction

Data reduction was carried out with GBTIDL (Marganian et al. 2006) v2.8 for GBT13A-468 and v2.10.1 for GBT18B-

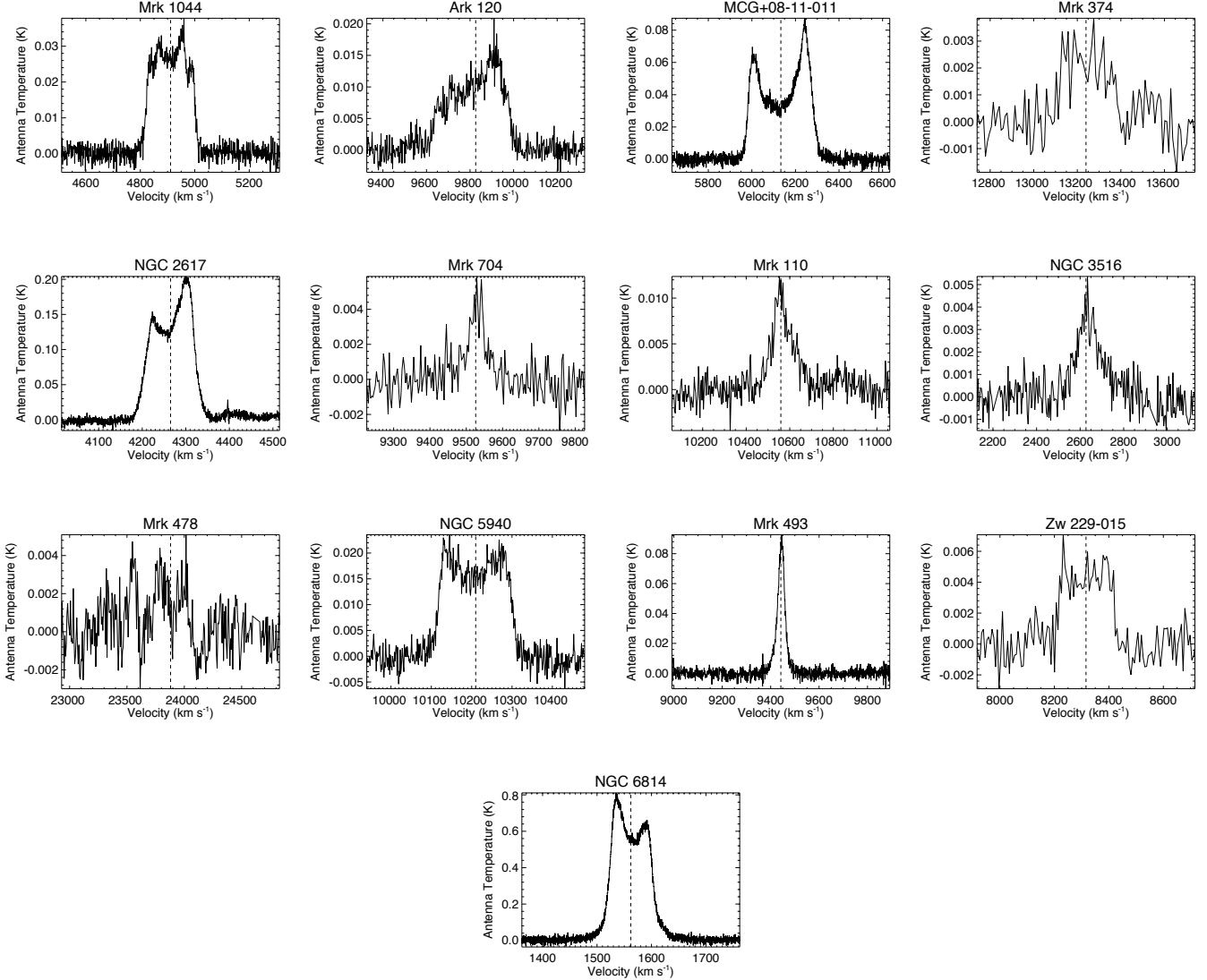


**Figure 2.** HI emission line spectra from GBT18B-258 after reduction, baseline subtraction, and smoothing with GBTIDL v2.10.1. Hanning smoothing was applied to all profiles, and further smoothing was dependent on the S/N (see Sec. 2.2). The vertical dashed lines indicate  $V_R$  measurements from `gmeasure`.

258. The updated software includes the ability to reduce spectra taken with the VEGAS backend, as well as bug fixes. Individual scans were visually inspected, and those which contained significant saturation from RFI were removed. The `getps` GBTIDL procedure retrieved the on-source and corresponding off-source data for each scan pairing and performed the (ON-OFF)/OFF operation. Scans were then accumulated and averaged over for each target. Weaker RFI spikes were manually removed by interpolating over the interference in the accumulated spectra. Targets that required several hours of exposure time were generally observed in separate blocks across a few days. Scans from separate observing sessions were managed in the same way; all scans from each observation block of the same source were accumulated and averaged at once into a single spectrum.

We fit a low-order polynomial (typically order 3) to the remaining baseline in each combined spectrum and subtracted it. Hanning smoothing (Hann 1903) was then applied to all spectra after accumulation and baseline subtraction. Hanning smoothing is a running mean across the spectrum that aids in

reducing the ringing produced by strong RFI sources and reduces the spectral resolution by a factor of 2. Higher order smoothing was then applied to spectra with low apparent S/N to aid in the measurement of the emission line properties.

We detected HI 21 cm emission in 18 of the 27 targets from GBT13A-468 and in 13 out of 17 for GBT18B-258. Some of the more distant objects in the sample with  $z > 0.05$  resulted in non-detections within the allotted exposure time. Figs. 1 and 2 show the reduced, smoothed, and baseline subtracted spectra for targets where HI emission was detected from programs GBT13A-468 and GBT18B-258, respectively. We report in Table 2 the total resulting on-source exposure times after removal of contaminated scans, an approximate S/N for all spectra, values for the root-mean-square (RMS) of the noise in each spectrum, the final velocity resolution after smoothing, and the corresponding backend. For dual-horned profiles, approximate S/N values were calculated first by taking the average of the peak fluxes in each horn. We then averaged that with the mid-profile peak flux, and divided by the RMS of the noise to produce the approximate S/N. For Gaussian profiles,

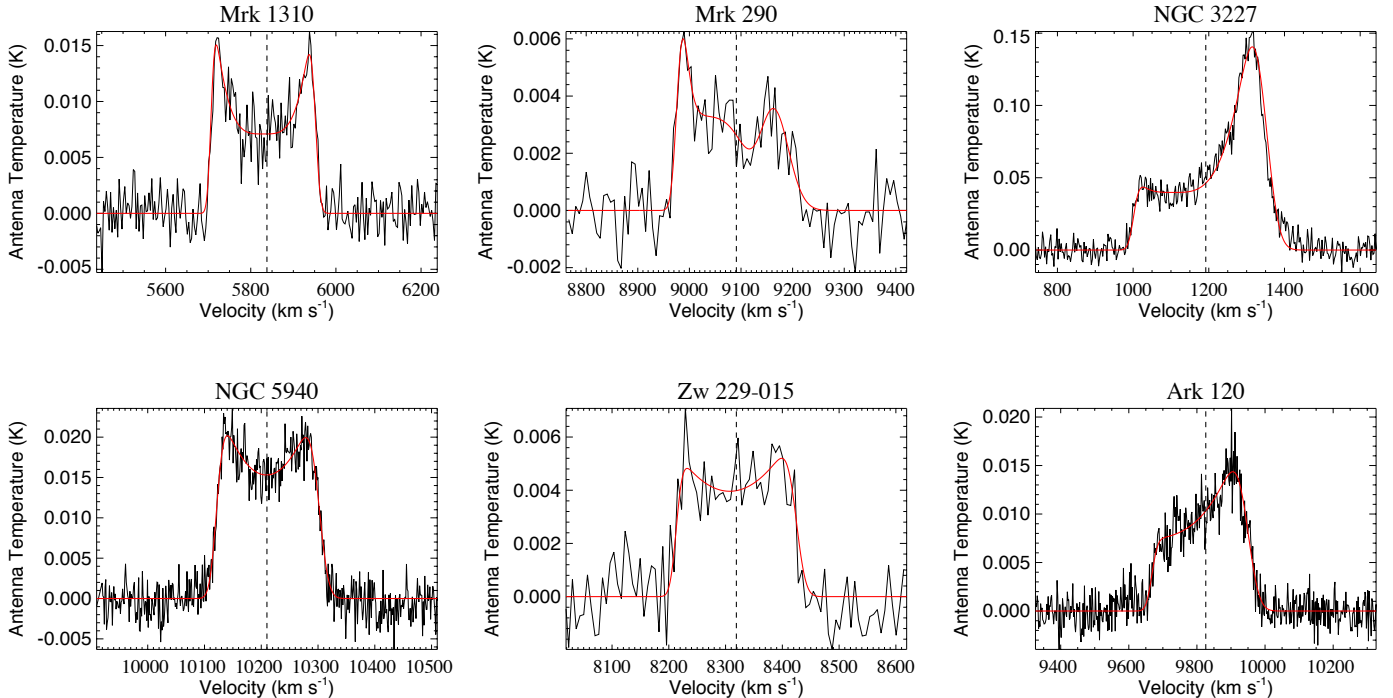


**Figure 3.** Example BUSYFIT (Westmeier et al. 2014) profiles for representative galaxies in our sample. The data is in black, the model fit is the solid red curve. The top row are profiles from GBT13A-468, the bottom are profiles from GBT18B-258. The vertical dashed lines indicate  $V_R$  measurements from BUSYFIT.

the approximate S/N was calculated as the peak flux value divided by the RMS of the noise.

### 2.3. Analysis and Measurements

Measurements of the emission-line widths, center-line recessional velocities ( $V_R$ ), and integrated line fluxes were determined with two methods. The first method utilized the `gmeasure` procedure available within GBTIDL, which calculates line widths, fluxes, and recessional velocities directly from the data. For width measurements, the `gmeasure` procedure determines the edges of an emission profile by linear interpolation over channels containing the profile until the data are greater than the provided threshold. The threshold is normally 50% or 20% times the mean flux over the range of channels containing the HI signal.  $W_{50}$  and  $W_{20}$  values (line widths at 50% and 20%, respectively) as well as  $V_R$  values are provided in  $\text{km s}^{-1}$ . We choose the mean flux, rather than the peak flux, for determination of  $W_{50}$  and  $W_{20}$  because it is less sensitive to the noise level, especially when a profile consists of significantly asymmetric peak horn fluxes. Calculated line fluxes are given in terms of antenna temperature ( $T_L$ ; see Section 3) in  $\text{K km s}^{-1}$ . Uncertainties on the `gmeasure` measurements were achieved using a bootstrap method. We began by defining beginning and ending spectral channel windows on either side of the line profile. The designated range of channels for each window on each side was unique to each profile and was mainly dependent on the noise properties (see Table 2), but was typically  $\sim 50$  channels in width. We then performed 100,000 iterations in which a starting and ending wavelength were randomly drawn from the defined windows, and a line width, flux, and central velocity were calculated using `gmeasure`. A distribution of each measurement was built up in this way, and we report the median of the distribution as the measurement value and the measurement uncer-

tainty as the  $1\text{-}\sigma$  deviation from the median on each side of the distribution, allowing for asymmetric distributions.

The second method employed the BUSYFIT software (Westmeier et al. 2014). For well-defined profiles, BUSYFIT is able to automatically determine the best-fit parameterization, but for noisy or poorly-defined profiles, additional user intervention is necessary. Measurements of  $W_{50}$  and  $W_{20}$ , (which in this case are defined as line widths at 50% and 20% of the peak flux density, which differs slightly from the definition employed by `gmeasure`),  $T_L$ , and  $V_R$  are derived from the BUSYFIT profiles. For both methods, we define  $V_R$  in the optical convention ( $c(\lambda-\lambda_0)/\lambda_0$ ). The fitting function has the form

$$B(x) = \frac{a}{4} \times (\text{erf}[b_1\{w+x-x_e\}] + 1) \times (\text{erf}[b_2\{w-x+x_e\}] + 1) \times (c|x-x_p|^n + 1) \quad (1)$$

where  $x$  denotes the spectral axis input,  $a$  is the amplitude scaling factor, the error functions fit the sides of the HI profile (flanks),  $b_1$  and  $b_2$  are the independent slopes of the flanks allowing for asymmetric shapes of the lines to be fit,  $w$  is the half-width of the HI profile,  $x_e$  and  $x_p$  are separate offsets also aiding in fitting asymmetric profile shapes, and  $c$  denotes the amplitude of the central trough of the profile relative to the flanks which is fit with a polynomial of degree  $n$ .

The majority of the dual-horned profile fits converged without the need to hold any free parameter values fixed. Most well-defined, Gaussian-shaped profiles also achieved convergence in the fit. For these, BUSYFIT automatically fixes the parameters included in the central trough factor of the fitting function ( $c$ ,  $x_p$ , and  $n$ ) at 0. We found it common that low S/N or weakly defined dual-horned profiles required holding the  $c$  and  $n$  values fixed because the initial fits often converged to Gaussian shapes. We also found common that narrow, low

S/N Gaussian profiles required holding at least one of the flank slopes fixed as the initial fits resulted in either extremely high uncertainties in these parameters or did not reach convergence. Generally in the cases which necessitated parameters to be held fixed, we inferred the values from the fits for well-defined profiles which converged automatically. We assessed by eye the accuracy of the shape of the fit relative to the inherent shape of the emission line, and we estimate the following additional uncertainties on each parameter:  $n$ :  $\pm 15\%$ ,  $c$ :  $\pm 29\%$ ,  $w$ :  $\pm 4\%$ ,  $b_1$ :  $\pm 21\%$ ,  $b_2$ :  $\pm 22\%$ ,  $x_p$ :  $\pm 8.5\%$ .

BUSYFIT offers a number of methods for determining uncertainties. We employed the Monte Carlo method which generates 10,000 best fits by randomly varying the free parameters in each iteration. The variations are dependent on the covariance matrix of the values of the free parameters, with each parameter's random distribution centered on the initial fit value and standard deviation derived from the square root of the diagonal elements of the covariance matrix. The uncertainties are assumed to be symmetric and are reported as the standard deviation from the mean of the resulting measurement distribution. For uncertainty determinations on fits in which parameters were held fixed, there is a tendency for underestimations due to the fixed parameters not contributing to uncertainty propagation. To account for this, we conducted best fits on SBS1116+583A (the lowest S/N HI profile in which no parameters were held fixed for the reported BUSYFIT measurements), fixing each free parameter and each combination of fixed free parameters to calculate the differences in resulting uncertainties from the initial fit's uncertainties. We then inflated the measurement uncertainties by a corresponding amount to match the differences on SBS1116+583A for objects with parameters that were held fixed in the fitting process.

Fig. 3 displays the best-fit BUSYFIT profiles overlaid on the HI spectra for a few representative galaxies. Profiles from GBT13A-468 are displayed in the top row, and profiles from GBT18B-258 in the bottom row. Table 3 reports the measured values of  $T_L$ ,  $W_{50}$ ,  $W_{20}$ , and  $V_R$  from `gmeasure` and from BUSYFIT. Comparisons between all measurements from `gmeasure` and BUSYFIT are shown in Fig. 4. Measurements from GBT13A-468 are shown in solid black circles, and GBT18B-258 are shown in open blue circles. A line of unity is shown in each panel, and the differences between the two methods' measurements are shown below each panel. The results are generally in close agreement even though the definitions of the line widths are slightly different, with only a few objects showing large discrepancies. NGC 3227, in particular, has a highly asymmetric line profile with a low central trough and blueshifted horn. This makes the determination of  $W_{50}$  quite sensitive to the noise in the spectrum, and whether 50% of the peak flux is below or above the blueshifted horn. If we choose the peak flux definition for `gmeasure`'s  $W_{50}$  measurement, we find a more consistent value with BUSYFIT. Both MCG-06-30-15 and Mrk 478 show some disparities in their line widths due to the low S/N in their spectra. And for Gaussian-shaped profiles, like those seen in Mrk 279, NGC 5548, Mrk 704, Mrk 110, NGC 3516, and Mrk 493, the two methods are more likely to disagree due to the difficulty in determining the true edges of the profiles. We also note that three of our spectra (NGC 4051, NGC 4593, NGC 5548) exhibit the surprising feature of excess HI emission at or near the systemic velocity. For the remaining analysis, we prefer the measurement values from `gmeasure` due to their asymmetric distributions more accurately reflecting the asymmetric

nature of the majority of the profiles.

#### 2.4. Notes on Individual Objects

Of the 31 galaxies with HI detections in our sample, 12 have not been previously studied in HI. For the remaining objects, we have tabulated their previous measurements for comparison with our own in Table 4. Below, we include a short discussion of the different measurements for each object. We also include discussion on the best-fit models produced by BUSYFIT whenever user intervention was necessary.

Two of the objects in this study, Mrk 6 and NGC 7469 (see Fig. 1) exhibit a strong center-line absorption feature in their HI profiles. While the absorption does not affect their line widths or recessional velocities, it does affect the line flux. In order to estimate a reasonable range of values for the unabsorbed line flux, we used a bootstrapping interpolation method. We first determined the ratios of horn-height to mid-profile-height from all of the unabsorbed dual-horned profiles in our sample. We then designated the lowest and highest ratios (0.16 and 0.52, respectively) as the acceptable range of flux values for the underlying unabsorbed central trough in the line profiles of Mrk 6 and NGC 7469. We then linearly interpolated over the central absorption with 100,000 random draws between the minimum and maximum allowed trough height. For each iteration, the total line flux was recorded, thereby building up a distribution of likely unabsorbed line flux measurements. The median of the resulting distribution is reported as the final  $T_L$  value, and the uncertainties reflect the 1- $\sigma$  deviation from the median on either side of the distribution.

While the optical angular extents of all galaxies with HI detections in our sample are encompassed by the 9'.1 GBT beam, the total extent of the HI distribution of the closest objects may not be. We examined resolved HI maps to verify the angular HI extent of the nearest galaxies in our sample, whenever such maps were available in the literature.

Mrk 1044: The emission profile for this galaxy contains several flux peaks between the flanks (see Fig. 2). This caused the initial BUSYFIT model to fit the flank slopes while converging with a value of 0 for the central trough amplitude. In order to fit a weak dual-horn signature, we held the trough amplitude ( $c$ ) fixed at 0.0001, the trough offset ( $x_p$ ) fixed at 235, and the polynomial degree ( $n$ ) fixed at 2. For this object, Mirabel & Wilson (1984) employed the National Radio Astronomy Observatory (NRAO) 91 m telescope's 384 channel autocorrelation spectrometer with 11 km s<sup>-1</sup> channel spacing and velocity resolution of 22 km s<sup>-1</sup>. The spectrum reported by Mirabel & Wilson (1984) contains a noise spike close to the redshifted side of the HI profile. The inclusion of the noise spike as part of the HI profile, due to low S/N and low resolution, is the most probable cause for the large discrepancy between their  $W_{20}$  measurement of 489 km s<sup>-1</sup> and ours of 196.2<sup>+4.3</sup><sub>-10.4</sub> km s<sup>-1</sup> and the slight offset in their  $V_R$  value of 4932 km s<sup>-1</sup> compared to ours of 4910.77<sup>+0.69</sup><sub>-1.35</sub> km s<sup>-1</sup>. Measurements made by König et al. (2009) based on observations with the Effelsberg 100 m telescope's 8,192 channel autocorrelator are consistent with our measurements.

Ark 120: The profile of Ark 120 has a slightly skewed dual-horn shape (see Fig. 2). Theureau et al. (2005) conducted an observation using the Nançay 94 m telescope with an 8,192 channel autocorrelation spectrometer, which resulted in an HI detection with S/N=3.8. The low S/N in the Theureau et al. (2005) observations would make it difficult to fully character-

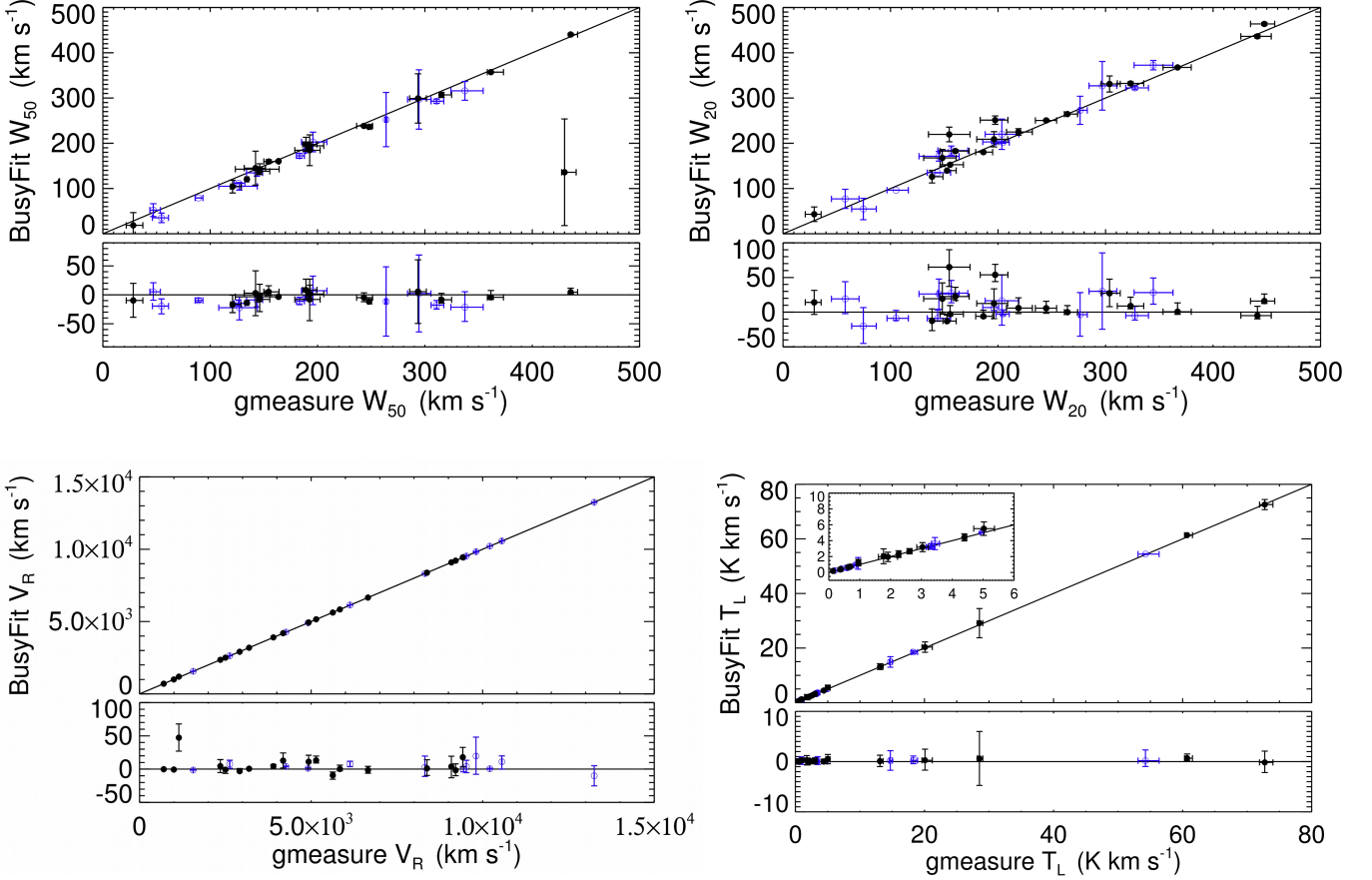


**Figure 4.** Comparison of the measurements from `gmeasure` and `BUSYFIT`:  $W_{50}$  (top left),  $W_{20}$  (top right),  $V_R$  (bottom left), and  $T_L$  (bottom right). The solid line in each panel is a line of unity, and `BUSYFIT` minus `gmeasure` is plotted below each panel. Measurements of profiles from GBT13A-468 are shown in solid, black circles, and measurements from GBT18B-258 are shown in open, blue circles. The outlier in the top left plot is NGC 3227 (see Fig. 1, Sec. 2.4), which exhibits a lopsided profile, resulting in significant uncertainty in the  $W_{50}$  line width measurement due to the uncertainty on the exact value of 50% peak flux.

ize the weaker, blueshifted side of the line profile, and likely accounts for the discrepancies between their reported measurements and ours. Where they find values of  $W_{50}=194 \pm 33$  km s<sup>-1</sup>,  $W_{20}=233 \pm 50$  km s<sup>-1</sup>, and  $V_R=9807 \pm 17$  km s<sup>-1</sup>, we report values of  $W_{50}=337.3^{+17.0}_{-13.1}$  km s<sup>-1</sup>,  $W_{20}=344.4^{+18.4}_{-17.9}$  km s<sup>-1</sup>, and  $V_R=9806.38^{+9.22}_{-4.51}$  km s<sup>-1</sup>. On the other hand, [Ho et al. \(2008a\)](#) report values of  $W_{20}=370.3 \pm 6.8$  km s<sup>-1</sup> and  $V_R=9809.2 \pm 3.4$  km s<sup>-1</sup> that are fairly consistent with our measurements within the uncertainties.

MCG+08-11-011: [Mirabel & Wilson \(1984\)](#) observed this target with the NRAO 91 m telescope, which was then reprocessed ([Springob et al. 2005](#)) for inclusion in the Extragalactic Distance Database (EDD; [Tully et al. 2009a](#)). Both  $V_R$  measurements (6146 and 6133 km s<sup>-1</sup>, respectively) and the reprocessed width measurement ( $310 \pm 15$  km s<sup>-1</sup>) are consistent with our measurements of  $V_R=6133.26^{+1.31}_{-1.04}$  and  $W_{50}=310.8^{+6.7}_{-5.1}$  km s<sup>-1</sup>.

Mrk 374: Mrk 374 has a relatively faint emission line (see Fig. 2) and we were only able to achieve a S/N of 4.7. The initial `BUSYFIT` profile converged into a box-shaped best fit with a value of 0 for the central trough amplitude. In order to generate a trough feature while keeping the slopes of the flanks accurate, we held fixed the initial best fits to the flank slopes ( $b_1$  and  $b_2$ ) at 0.8, 0.5, respectively. We then fixed the central trough amplitude ( $c$ ) at 0.01 and polynomial de-

gree ( $n$ ) at 1.5, which allowed a double horned profile shape to converge. Mrk 374 was previously observed by [Davoust & Contini \(2004\)](#) with the 512 channel autocorrelator on the Nançay telescope. They defined their recessional velocities in the radio convention ( $c(\lambda-\lambda_0)/\lambda$ ) instead of the optical convention ( $c(\lambda-\lambda_0)/\lambda_0$ ), which we have used in this work. The recessional velocity reported for Mrk 374 by [Davoust & Contini \(2004\)](#) of  $12780 \pm 8$  km s<sup>-1</sup> is equivalent to  $13349$  km s<sup>-1</sup> in the optical convention, as compared to our measurement of  $13250.00^{+0.07}_{-0.06}$  km s<sup>-1</sup> in the optical. They report a S/N of 6.9 with an integrated flux of  $8.54$  Jy km s<sup>-1</sup>, which is equivalent to  $17.08$  K km s<sup>-1</sup>, much higher than our flux of  $0.59^{+0.02}_{-0.01}$  K km s<sup>-1</sup>. Their width measurements also consist of significant discrepancies relative to ours; they list  $W_{50}=74 \pm 16$  km s<sup>-1</sup> and  $W_{20}=121 \pm 24$  km s<sup>-1</sup>, as opposed to our reported values of  $W_{50}=263.8^{+0.9}_{-1.0}$  and  $W_{20}=276.3^{+6.6}_{-0.9}$  km s<sup>-1</sup>. However, their spectrum contains a strong Gaussian-shaped signal unlike the faint dual-horned profile which we report. [Davoust & Contini \(2004\)](#) discuss that observations at recessional velocities near  $\sim 12500$  km s<sup>-1</sup> (in the radio convention) contained significant interference from radar signals, and that galaxies in their sample near those velocities are possibly unreliable. Therefore, it is possible that the target was misidentified in their work.

Mrk 79: Two previous observations of this object with

the GBT are reported in the HI Digital Catalog of [Springob et al. \(2005\)](#). Each observation reports a  $W_{50}$  value ( $169 \pm 15$ ,  $155 \pm 7$  km s<sup>-1</sup>) and a recessional velocity ( $6657$ ,  $6659 \pm 5$  km s<sup>-1</sup>), and they are consistent with our measurements of  $W_{50} = 154.4_{-4.5}^{+9.7}$  and  $V_R = 6657.41_{-3.88}^{+4.76}$  km s<sup>-1</sup> within the uncertainties.

NGC 2617: Previous observations include the Nançay telescope ([Paturel et al. 2003](#)) and the Parkes telescope including two measurements from the HI Parkes All Sky Survey Catalogue ([Meyer et al. 2004](#); [Doyle et al. 2005](#)). The HI data for NGC 2617 was also reprocessed ([Theureau et al. 2006](#)) for inclusion in the EDD. All previous reported measurements are in agreement with our measurements.

Mrk 704: Mrk 704 has a narrow Gaussian emission profile shape (see Fig. 2). The BUSYFIT central trough, offset, and polynomial parameters ( $c$ ,  $x_p$ , and  $n$ ) were thus automatically fixed at 0, and we also held the left flank slope ( $b_1$ ) fixed at 0.15 to allow the profile to converge. The spectrum reported by [Hutchings \(1989\)](#) from observations with the Arecibo telescope contains a very low S/N emission line blended with a noise spike on the blueshifted side. The larger  $W_{20}$  value they report of 250 km s<sup>-1</sup> compared to ours of  $57.8_{-12.9}^{+12.8}$  km s<sup>-1</sup> is possibly due to the nearby noise spike's inclusion in the profile measurement. This would also explain the slight offset in their  $V_R$  value of 9510 km s<sup>-1</sup> compared to our measurement of  $9525.87_{-2.55}^{+1.60}$  km s<sup>-1</sup>.

NGC 3227: The blueshifted side of the profile of NGC 3227 is significantly weaker in flux than the redshifted side, resulting in a dramatically asymmetric shape (see Fig. 1). It is interacting with its neighboring galaxy NGC 3226 ([Tonry et al. 2001](#)), which is an elliptical galaxy, and in the resolved HI study by [Mundell et al. \(1995\)](#), they detected no HI emission from it. So while the interaction might be a possible explanation as to NGC 3227's skewed profile shape, NGC 3226 most likely does not contribute to the emission profile we have detected. The spectral resolution of the previously published spectra range from 6.6 km s<sup>-1</sup> ([Dickel & Rood 1978](#)) from observations which used the 91 m telescope at the NRAO to 30 km s<sup>-1</sup> ([Biermann et al. 1979](#)) for observations with the 305 m Arecibo telescope. The  $V_R$  measurement of  $1284 \pm 9$  km s<sup>-1</sup> reported by [Dickel & Rood \(1978\)](#) presents the biggest discrepancy with our  $V_R$  measurement of  $1144.74_{-0.82}^{+4.33}$  km s<sup>-1</sup>. The baseline in their spectrum contains significant residual fluctuations and possible source confusion; it appears the S/N in their spectrum is too low for identification of the blueshifted side of the profile. Our spectral resolution of 3.0 km s<sup>-1</sup> is higher than all previous spectra, and our higher S/N of 13.1 allows for clear identification of the entire profile. Our measurements of  $W_{20}$  and  $V_R$  are consistent with [Ho et al. \(2008a\)](#) within the uncertainties. [Martin \(1998\)](#) report a maximum HI angular diameter of NGC 3227 of 5' based on the resolved study by [Mundell et al. \(1995\)](#), therefore the total 21 cm emission is most likely enclosed by the 9'1 GBT beamwidth.

NGC 3516: This is the first HI spectrum for NGC 3516, a relatively nearby galaxy, due to the extreme faintness of its HI emission. The total on-source observing time spent on this object was longer than any of our other targets by a large margin ( $\sim 15.6$  hours). The HI profile of NGC 3516 exhibits a Gaussian shape, and as such the BUSYFIT model held the central trough amplitude, offset, and polynomial degree parameters ( $c$ ,  $x_p$ , and  $n$ ) fixed at 0. We also held the right flank slope ( $b_2$ )

fixed at 0.1 to allow the profile fit to converge.

NGC 3783: Previous HI line widths are derived from observations with the Nançay telescope ([Theureau et al. 2006](#)) and reprocessed for inclusion in the EDD ([Tully et al. 2009b](#)). Our values for  $W_{50}$ ,  $W_{20}$ , and  $V_R$  are consistent within the uncertainties.

NGC 4051: Our reported measurements of  $W_{50}$  and  $W_{20}$  are consistent with those of [Fisher & Tully \(1981\)](#), obtained from the NRAO 91 m telescope and reanalyzed for inclusion in the EDD. [Dickel & Rood \(1978\)](#), who used the same instrument as [Fisher & Tully \(1981\)](#), defined their profile widths as the half-width between points at one-quarter peak intensity corrected for the spectral resolution of the instrument of 6.6 km s<sup>-1</sup>. Their reported value (doubled to achieve a full width at quarter intensity) of 268 km s<sup>-1</sup> is consistent with our similar measurement of  $W_{20} = 264.5_{-2.9}^{+9.5}$  km s<sup>-1</sup>. All previous  $V_R$  measurements are consistent with our measurements. The resolved HI study of [Liszt & Dickey \(1995\)](#) reveals the diameter of the major axis is similar to that of the optical diameter at 5/2, therefore it is expected that all the HI emission is contained within the 9'1 GBT beam.

NGC 4151: Our measurements of  $W_{50}$  and  $W_{20}$  are approximately consistent with the values reported by [Tift & Cocke \(1988\)](#). The small discrepancies of  $\sim 3 - 10$  km s<sup>-1</sup> most likely come from the difference in spectral resolution, channel span, and channel spacing. For relatively flat baselines such as that present in our spectrum of NGC 4151, low-order polynomial fits can possibly introduce low-level sinusoidal structure in the baseline. This can affect subsequent measurements and/or fits to the emission profile, and can thus result in small discrepancies in reported measurements. The NRAO 91 m telescope employed by [Tift & Cocke \(1988\)](#) produced a spectrum for NGC 4151 with a resolution of 11 km s<sup>-1</sup> over 192 channels. As with NGC 4051, [Dickel & Rood \(1978\)](#) defined their width as the half-width between points at quarter-intensity corrected for a spectral resolution of 6.6 km s<sup>-1</sup>. Their reported value (doubled to match a full width) of 156 km s<sup>-1</sup> is consistent with our measurement of  $W_{20} = 152.5_{-0.7}^{+8.5}$  km s<sup>-1</sup>. The previous  $V_R$  measurements are consistent with our measurements. In their neutral hydrogen study of NGC 4151, [Pedlar et al. \(1992\)](#) report the extent of the spiral arms reach  $\sim 6'$  from its center, and the reanalysis of the same study by [Martin \(1998\)](#) from their compiled catalog of HI maps report the largest angular extent of the neutral hydrogen as 10/4. The 9'1 beam of the GBT may not fully enclose the total extent of the HI emission from NGC 4151, but only a small fraction is likely to have been missed.

Mrk 766: Mrk 766 has a low S/N emission line (5.1; see Fig. 1) with a very faint dual-horn signature. With all eight BUSYFIT parameters free, the initial fit was Gaussian in shape. In order to fit the weak horns, the right flank slope ( $b_2$ ) was held fixed at 0.45 in addition to the polynomial degree ( $n$ ) which was fixed at 2. There are no previous measurements of the HI emission from this galaxy.

NGC 4593: Observations conducted by [Staveley-Smith & Davies \(1987\)](#) and [König et al. \(2009\)](#) employed the Jodrell Bank 76 m MkIA radio telescope's 1024 channel autocorrelation spectrometer with a velocity resolution of 7.3 km s<sup>-1</sup> and the Effelsberg 100 m telescope's 8,192 channel autocorrelator with a velocity resolution of 4.1 km s<sup>-1</sup>, respectively. Our reported resolution is 0.6 km s<sup>-1</sup>, and our width and velocity measurements are consistent with theirs. NGC 4593 is also composed of many morphological components including an



outer ring and a bar, which is a possible explanation for the fluctuating HI emission between the horns of its profile.

MCG-06-30-015: The HI measurements in this work are the first reported for this galaxy. MCG-06-30-015 has one of the faintest emission lines that was detected ( $S/N=3.4$ ) in our sample. To fit the asymmetric dual-horned profile, we held the central trough amplitude ( $c$ ) fixed at 0.011, the half-width ( $w$ ) fixed at 5, and the polynomial degree ( $n$ ) fixed at 2.8.

NGC 5548: Within the uncertainties, our measurement of  $W_{50}$  is consistent with that of [Stierwalt et al. \(2005\)](#) based on observations with the Arecibo telescope, with a  $S/N$  of 4.1 and spectral resolution of  $8.5 \text{ km s}^{-1}$ . The spectrum reported by [Biermann et al. \(1979\)](#), also from Arecibo, has a low resolution of  $30 \text{ km s}^{-1}$ , as opposed to our smoothed velocity resolution of  $4.8 \text{ km s}^{-1}$ , leading to significant ambiguity in identification of the edges of their profile and their subsequent  $W_{50}$  measurement of  $110 \text{ km s}^{-1}$ , compared to our  $W_{50}$  measurement of  $189.1^{+10.3}_{-3.0} \text{ km s}^{-1}$ . In the spectrum reported by [Mirabel & Wilson \(1984\)](#) from Arecibo, with a velocity resolution of  $22 \text{ km s}^{-1}$  and channel spacing of  $11 \text{ km s}^{-1}$ , the profile exhibits an extended, low-amplitude blueshifted wing, possibly leading to the discrepancy in their  $W_{20}$  measurement of  $472 \text{ km s}^{-1}$  in comparison to our  $W_{20}$  measurement of  $197.3^{+11.8}_{-14.0} \text{ km s}^{-1}$ . The same issue is present in the spectrum reported by [Ho et al. \(2008a\)](#) (velocity resolution of  $5.15 \text{ km s}^{-1}$ ), leading to disagreement between their  $W_{20}$  measurement of  $321.1 \pm 6.8 \text{ km s}^{-1}$  and our  $W_{20}$  measurement. After smoothing our spectrum to match the lower velocity resolution of  $22 \text{ km s}^{-1}$ , we arrive at a  $W_{20}$  measurement of  $270 \text{ km s}^{-1}$ , closer to the larger values of [Mirabel & Wilson \(1984\)](#) and [Ho et al. \(2008a\)](#). Our  $V_R$  value is within the range of reported values. The deep optical imaging of NGC 5548 by [Tyson et al. \(1998\)](#) reveals a low surface brightness arm wrapping around the galaxy, an extended tail, and ripples in the inner disk, all of which could contribute to the highly turbulent HI flux distribution present in our spectrum.

Mrk 478: There are multiple emission peaks near the expected location of HI emission from Mrk 478 (see Fig. 2), which is between  $22484 - 23700 \text{ km s}^{-1}$  ([Richards et al. 2009](#); [de Vaucouleurs et al. 1991](#)) from recessional velocities measured from optical emission lines. The systemic velocity of Mrk 478 is not well constrained, and we do not detect emission at or near the low end of its range of optical velocities. We fit independent Gaussians to the three peaks present in our spectrum to compare to the systemic velocities of galaxies in the NASA/IPAC Extragalactic Database (NED) in a  $9'1$  diameter neighbor search (equal to the GBT L-Band beam size). We measure the following velocities for each peak (from left to right):  $23540 \pm 11$ ,  $23800 \pm 15$ , and  $23980 \pm 4 \text{ km s}^{-1}$ . The left peak's velocity is comparable to the nearby galaxy 2MASX J14415920+3527489 ( $V_R=23554 \text{ km s}^{-1}$ ;  $2'2$  to the NW). Our  $V_R$  measurement for the center peak is near the reported velocities of neighboring galaxies 2MASX J14421361+3524459 ( $V_R=23738 \text{ km s}^{-1}$ ;  $2'3$  to the SW) and 2MASX J14421426+3528139 ( $V_R=23763 \text{ km s}^{-1}$ ;  $2'3$  to the NE). Lastly, within a  $9'1$  diameter neighbor search, there are no objects classified as galaxies near our measured velocity of the right peak. From the present information, it is unclear whether Mrk 478 exhibits a dual-horned shape, and it is also unclear as to which of the peaks represent emission from Mrk 478. Based on the similarity of the center and right peak's shape with that of the measured shapes of low  $S/N$

dual-horned profiles, as seen with other objects in our sample (SBS1116+583A, Mrk 817, Mrk 290), we have assumed the center and right peaks belong to the emission profile of Mrk 478. For analysis with BUSYFIT, we fixed the slope of the right flank ( $b_2$ ) at 0.26, the half-width parameter ( $w$ ) at 23, and the polynomial degree ( $n$ ) at 3 in order to achieve a characteristic dual-horned fit. [Teng et al. \(2013\)](#) observed Mrk 478 with the 100 m GBT (identified as PG 1440+356 in their work), producing a spectrum with a resolution of  $\sim 6 \text{ km s}^{-1} \text{ channel}^{-1}$  and  $S/N$  of 4.81. The large absorption feature present in their spectrum at  $\sim 24000 \text{ km s}^{-1}$  is absent from ours. [Teng et al. \(2013\)](#) note that the feature has a dramatic variability over short timescales and is also dependent on polarization, and their Figure 6 shows strong continuum fluctuations on month-long periods. They report measurements of  $W_{50}=395 \pm 26$ ,  $W_{20}=477 \pm 39$ , and  $V_R=23406 \pm 13 \text{ km s}^{-1}$ , which differ significantly from our values of  $W_{50}=294.5^{+11.1}_{-10.6}$ ,  $W_{20}=296.9^{+13.6}_{-12.3}$ , and  $V_R=23879.90^{+5.54}_{-5.26} \text{ km s}^{-1}$ . It is possible that they assumed the left peak was part of the HI emission from Mrk 478, leading to the discrepancy between their measurements and our measurements. If we include all three peaks in our measurement, we find a  $W_{50}$  value of  $476^{+12}_{-10} \text{ km s}^{-1}$ , a  $W_{20}$  value of  $477^{+12}_{-12} \text{ km s}^{-1}$ , and a  $V_R$  value of  $23752^{+6}_{-6} \text{ km s}^{-1}$ , closer to those of [Teng et al. \(2013\)](#).

NGC 5940: All previous measurements for NGC 5940 originate from observations with the Arecibo telescope, including a reprocessed measurement for inclusion in the EDD. The measurements conducted by [Lewis \(1983\)](#) contain consistent  $W_{50}$  and  $V_R$  values with our values, however their  $W_{20}$  value of  $240 \text{ km s}^{-1}$  is slightly higher than ours of  $204.5^{+5.9}_{-6.5} \text{ km s}^{-1}$ . The lower resolution of their spectrum ( $\sim 8.2 \text{ km s}^{-1}$ ) compared to ours of  $1.3 \text{ km s}^{-1}$  contributes to some of the discrepancy between the measurements, because we measure  $W_{20}=214 \text{ km s}^{-1}$  when we smooth our spectrum to match their resolution. However, we expect that the lower  $S/N$  in their spectrum also contributes to the difference in  $W_{20}$ . The remaining measurements from [Mirabel & Wilson \(1984\)](#), [Lewis \(1987\)](#), [Haynes et al. \(2011\)](#), [Springob et al. \(2005\)](#), and [Paturel et al. \(2003\)](#) are consistent with our measurements within the uncertainties.

Mrk 493: The HI profile of Mrk 493 exhibits a strong, narrow Gaussian shape (see Fig. 2). As standard for fitting a Gaussian-shaped profile, the BUSYFIT parameters controlling the central trough amplitude, offset, and polynomial degree ( $c$ ,  $x_p$ , and  $n$ , respectively) were set to 0, and we found that we also needed to hold the half-width parameter ( $w$ ) fixed at 10 to allow the profile fit to converge. All previous observations utilized the 305 m Arecibo telescope. The  $V_R$  reported by [Haynes & Giovanelli \(1984\)](#) is consistent with our measurement, and their  $W_{50}$  value agrees with our measurement at the  $\sim 2 \sigma$  level. [Lewis \(1987\)](#) also reports a consistent  $V_R$  value. They define their  $W_{50}$  measurement of  $35.7 \text{ km s}^{-1}$  as an un-smoothed width, which might account for the discrepancy, yet it is consistent with our  $W_{50}$  of  $54.6^{+6.5}_{-8.4} \text{ km s}^{-1}$  at the  $\sim 2 \sigma$  level. Values by [Mirabel & Wilson \(1984\)](#) are consistent with our measurements within the uncertainties.

1H1934-063: [Paturel et al. \(2003\)](#) report an HI line width of  $248.4 \pm 16.5 \text{ km s}^{-1}$  from observations with the Nançay telescope. Their spectrum contains significant baseline fluctuations, causing a discrepancy both between our width measurement and theirs and their  $V_R$  measurement of  $3070 \pm 7 \text{ km s}^{-1}$  compared to our value of  $V_R = 3191.42^{+0.06}_{-0.09} \text{ km s}^{-1}$ .

NGC 6814: [Mirabel & Wilson \(1984\)](#) observed this object with the NRAO 91 m telescope and the 192 channel autocorrelation spectrometer. The low spectral resolution of  $22 \text{ km s}^{-1}$  and channel spacing of  $11 \text{ km s}^{-1}$  possibly account for the slightly larger value of  $W_{20}$  that they report of  $134 \text{ km s}^{-1}$  compared to our value of  $105.1^{+11.4}_{-8.4} \text{ km s}^{-1}$ . All other previous measurements from [Shostak \(1978\)](#), [Koribalski et al. \(2004\)](#), [Springob et al. \(2005\)](#), [Huchtmeier & Richter \(1989\)](#) are consistent with our measurements. [Liszt & Dickey \(1995\)](#) estimate the HI diameter of NGC 6814 to be  $\sim 7'$  based on their resolved HI map, thus it is likely that the  $9'1$  GBT beam encompassed the total HI distribution of NGC 6814.

NGC 7469: Our data for NGC 7469 contained large baseline fluctuations across the whole continuum in a significant amount of the scans which were not included in the final, accumulated spectrum. The absorption profile present in the HI spectrum of NGC 7469 (see Fig. 1) persists throughout the literature, causing significant uncertainty in the line flux measurements. [Richter & Huchtmeier \(1982\)](#) utilized the Effelsberg 100 m telescope with spectral resolution of  $13.2 \text{ km s}^{-1}$  and channel spacing of  $11 \text{ km s}^{-1}$ , near insufficient to identify the emission profile separate from the noise level. Observations with the Arecibo telescope (e.g., [Mirabel & Wilson 1984](#); [Biermann et al. 1979](#); [Ho et al. 2008a](#)) all show self-absorption which is commented on in their analyses. [Biermann et al. \(1979\)](#), [Richter & Huchtmeier \(1982\)](#), and [Mirabel & Wilson \(1984\)](#) also comment on the galaxy companion IC 5283. NED lists the radial velocity of IC 5283 as  $4804 \text{ km s}^{-1}$ , very near the velocity of the blueshifted flank of NGC 7469, with an angular separation of only  $1/3$  (well within the GBT L-Band beam). Thus it is likely that most previous studies have the emission from this companion galaxy blended with that of NGC 7469. When comparing our spectrum to those of [Mirabel & Wilson \(1984\)](#), [Mirabel & Sanders \(1988\)](#), and [Ho et al. \(2008a\)](#), we note that their higher S/N spectra show an emission bump on the blueshifted wing of the profile, while our spectrum does not. It is likely that this feature is lost in the noise since we had to reject a large number of scans for this object. Consequently, we find a significantly different width for NGC 7469 than these previous studies. Reported  $W_{50}$  measurements are as follows:  $570 \text{ km s}^{-1}$  ([Biermann et al. 1979](#)) and  $515 \text{ km s}^{-1}$  ([Richter & Huchtmeier 1982](#)); previous  $W_{20}$  measurements consist of:  $525.1 \pm 6.8 \text{ km s}^{-1}$  ([Ho et al. 2008a](#)),  $583 \text{ km s}^{-1}$  ([Richter & Huchtmeier 1982](#)), and  $395 \text{ km s}^{-1}$  ([Mirabel & Wilson 1984](#)) We report measurements of  $W_{50} = 192.6^{+9.8}_{-13.9}$  and  $W_{20} = 196.2^{+12.7}_{-16.1} \text{ km s}^{-1}$ . The previous  $V_R$  measurements are consistent with our values within the uncertainties.

The literature on radial velocities and redshifts for the remaining objects in the sample consist of measurement methods that do not rely on 21 cm spectroscopy. For example, MCG-06-30-015 has a previous radial velocity measurement of  $2323 \pm 15 \text{ km s}^{-1}$  from the redshifting of infrared emission lines ([Fisher et al. 1995](#)). Based on the 21 cm emission, we report a measurement of  $V_R = 2353.53^{+4.15}_{-3.56} \text{ km s}^{-1}$ . Mrk 279 has measurements of  $V_R$  ranging from low estimates of  $8904 \pm 60 \text{ km s}^{-1}$  from the redshift of the strongest optical emission lines (e.g.,  $H\alpha$ , [O III]; [Osterbrock & Pogge 1987](#)), to high estimates of  $9600 \text{ km s}^{-1}$  from the redshift of the  $H\alpha$  emission line ([Arakelian et al. 1971](#)). Our measurement of  $V_R = 9211.71^{+8.29}_{-6.49} \text{ km s}^{-1}$  is contained within the wide range of previous values. Similarly, Mrk 817 has a range of  $V_R$

measurements from  $9275 \text{ km s}^{-1}$  ([Fouque et al. 1992](#)) to  $9430 \pm 35 \text{ km s}^{-1}$  (IRAS redshift survey; [Strauss & Huchra 1988](#)). Our measurement of  $V_R = 9420.14^{+4.08}_{-3.91} \text{ km s}^{-1}$  is in agreement with the higher end of these measurements. Table 5 lists the redshifts we have derived from our HI observations alongside previously published redshifts from a variety of observations and analysis methods.

### 3. DISTANCES AND MASSES

With the detection of HI 21 cm emission from 31 AGN host galaxies, we can explore the gas properties of these galaxies compared to their stellar and central black hole properties. We also augmented our sample by including the dwarf Seyfert NGC 4395, as it should provide an interesting comparison as the lowest-mass AGN with a direct black hole mass constraint, hosted by a bulgeless low surface brightness galaxy. We describe here our adopted measurements and derived quantities for the baryonic properties of the galaxies.

#### 3.1. Distances

Only five of the galaxies that we detected have distance measurements independent of their redshifts. The sources of the distances to NGC 3227, NGC 3783, NGC 4051, NGC 4151, and NGC 4593 are summarized in [Bentz et al. \(2013\)](#), but in brief, the measurements are generally the average of distances to galaxies within the same group, and were retrieved from the EDD. The exception is NGC 3227, which has an adopted distance that is the same as NGC 3226, with which it is interacting and which has a distance from the surface brightness fluctuation method ([Tonry et al. 2001](#)). These five galaxy distances have been recalibrated with a Hubble constant of  $H_0 = 72 \text{ km s}^{-1} \text{ Mpc}^{-1}$  for consistency with the Hubble Space Telescope (HST) Key Project ([Freedman et al. 2001](#)). Additionally, NGC 4395 has a distance from Cepheid variables ([Thim et al. 2004](#)) of  $4.1 \pm 0.4 \text{ Mpc}$ .

Many of the galaxies in our sample were included in [Bentz et al. \(2013\)](#) and [Bentz & Manne-Nicholas \(2018\)](#). For those objects, we adopt the luminosity distances ( $D_L$ ) reported in those works, which are derived from the redshifts of each galaxy. Uncertainties of  $500 \text{ km s}^{-1}$  were adopted due to the typical range of peculiar velocities reported by [Tully et al. \(2008\)](#).

For Mrk 1044, MCG+08-11-011, Mrk 374, NGC 2617, Mrk 704, Mrk 478, NGC 5940, Mrk 493, and 1H1934-063, we use our redshift measurement from the HI emission line to estimate  $D_L$ . For consistency with the other objects in our sample, we adopt an uncertainty of  $500 \text{ km s}^{-1}$  to account for peculiar velocities that may affect the distance derived from the redshift. Adopted distances are listed in Table 6.

#### 3.2. HI and Total Gas Mass

The integrated flux of the HI emission line allows the atomic gas mass to be estimated because the intensity from the spin-flip radiation of optically thin sources is related to the number of HI atoms in a  $1 \text{ cm}^2$  cross-section column. The measured flux is thus directly related to the total number of HI atoms in the beam, and the mass is given by

$$\frac{M_{HI}}{M_{\odot}} = [1.2 \times 10^5 D^2] \sum_{i=1}^n T_L(i) \Delta v \quad (2)$$

([Roberts 1962](#)), where  $D$  is the distance in Mpc (see Table 6), the summation is over channels spanning the HI emission-line profile, and  $\Delta v$  is the channel width in  $\text{km s}^{-1}$ .

The HI mass of a galaxy is then related to total gas mass as

$$M_{\text{GAS}} = 1.4M_{\text{HI}} \quad (3)$$

(Cox 2000). The scale factor of 1.4 accounts for the amount of atomic helium gas in the galaxy assuming solar abundance. As stated previously,  $\text{H}_2$  is the next most prevalent gas phase in disk galaxies. However, [McGaugh \(2012\)](#) revisited several molecular gas content estimation techniques (e.g., [Young & Knezek 1989](#)), and concluded that there is no compelling evidence for significant sources of baryonic matter in disk galaxies other than what can be directly detected through observations, and that the molecular gas contribution (in gas-rich spirals) is usually smaller than the uncertainty in the  $M_{\text{HI}}$  calculation. The uncertainties on the gas masses are primarily set by the uncertainties on the galaxy distances, but a small contribution also comes from the uncertainty on the integrated HI line flux. The  $M_{\text{GAS}}$  data used in [McGaugh \(2012\)](#) included uncertainties between 0.05 - 0.41 dex, consistent with what we find. Therefore, we assume that HI and helium accounts for approximately all significant gas mass contributions, with other phases and molecular gas providing a negligible contribution.

We derived  $M_{\text{GAS}}$  for NGC 4395 using the HI flux available in the All Digital HI Catalog ([Springob et al. 2005](#)) with Equations 2 and 3. The 140-foot Green Bank telescope was used to observe NGC 4395 and produce the subsequent HI flux we have used here. The beam size of the 140-foot is  $21'$ , large enough to encompass the angular extent of NGC 4395, therefore allowing use of Equation 2.

### 3.3. Stellar and Baryonic Mass

In order to derive baryonic masses, we adopt the stellar masses determined by [Bentz & Manne-Nicholas \(2018\)](#) for the majority of our targets. In that study, images in the  $V$  and  $H$  passbands from HST and the WIYN High-Resolution Infrared Camera, respectively, were modeled with GALFIT to separate the two-dimensional surface brightness components of the galaxy from the background sky and the AGN point source.  $V-H$  colors were derived from the fits to the galaxies and were used with the [Bell & de Jong \(2001\)](#) prescriptions to estimate the stellar mass-to-light (M/L) ratios, and therefore the stellar masses, of the galaxies. We adopt the stellar masses based on the [Bell & de Jong \(2001\)](#) prescriptions for the 22 galaxies in common between this work and that of [Bentz & Manne-Nicholas \(2018\)](#), and list them in Table 6.

For those objects in our sample that were not included in the [Bentz & Manne-Nicholas \(2018\)](#) study, we estimated the stellar masses based on in-hand data, magnitudes and colors taken from the literature, or a combination of the two. The stellar mass for NGC 5548 was determined from in-hand HST  $V$ -band and Apache Point Observatory<sup>4</sup>  $H$ -band images in the same manner as the [Bentz & Manne-Nicholas \(2018\)](#) sample. For MCG-06-30-015 and 1H1934-063, we estimated the stellar masses using the same method and prescription from [Bell & de Jong \(2001\)](#) with our in-hand HST  $V$ -band images combined with ground-based  $K$ -band images from the VISTA Hemisphere Survey<sup>5</sup> (VHS; [McMahon et al. 2013](#)).

The stellar masses for Mrk 704, NGC 5940, and Mrk 290 were estimated using the disk  $B-V$  colors reported by

<sup>4</sup> Based in part on observations obtained with the Apache Point Observatory 3.5 m telescope, which is owned and operated by the Astrophysical Research Consortium.

<sup>5</sup> Based on observations obtained as part of the VISTA Hemisphere Survey, ESO Program, 179.A-2010 (PI: McMahon.)

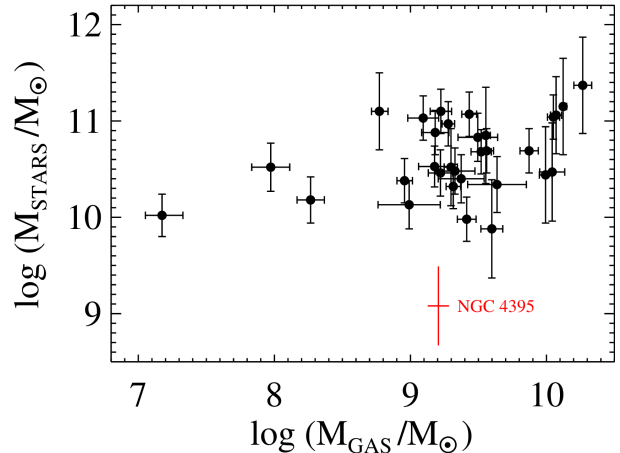


**Figure 5.** Comparison between  $M_{\text{GAS}}$  and  $M_{\text{STARS}}$ . There is a slight preference for gas mass to trace stellar mass, but the range of stellar masses is relatively small and the scatter is quite large.

[Granato et al. \(1993\)](#). The disk colors will not be affected by the central AGN; however, they will also be missing much of the color contributed by the bulge, which influences the total color and therefore the M/L ratio. Due to this limitation, we adopt an uncertainty of 0.28 mag on the colors. We then combined these colors with in-hand HST  $V$ -band magnitudes to estimate the stellar M/L ratios and thus stellar masses. We adopted a typical uncertainty of 0.2 mag for the HST  $V$ -band magnitudes, consistent with [Bentz & Manne-Nicholas \(2018\)](#).

The stellar masses for Mrk 1044, MCG-08-11-011, Mrk 374, NGC 2617, Mrk 478, and Mrk 493 were derived by first estimating the mean galaxy color based on their morphological types ([Buta et al. 1994](#), Table 6). For MCG-08-11-011, Mrk 374, NGC 2617, and Mrk 478, we then combined the estimated color with in-hand HST  $V$ -band magnitudes to estimate the stellar M/L ratio using the [Bell & de Jong \(2001\)](#) prescriptions, and thus constrain the total stellar mass. In the cases of Mrk 1044 and Mrk 493, where we did not have  $V$ -band HST imaging in hand, we utilized the surface brightness decompositions of [Wang et al. \(2014\)](#) to determine the fraction of the AGN luminosity to the total galaxy luminosity. We then corrected the total  $V$ -band magnitudes of these galaxies reported by [MacKenty \(1990\)](#) for the estimated contributions of the central AGNs. Combined with the galaxy color estimated from the morphological type, we were able to estimate the stellar M/L and thus the total stellar mass. For the HST  $V$ -band magnitudes, we adopted a typical uncertainty of 0.2 mag. For the mean galaxy colors and magnitudes from [MacKenty \(1990\)](#), we conservatively adopted uncertainties of 0.35 mag and 0.25 mag, respectively.

We derived the stellar mass for NGC 4395 using the integrated  $B$ -band magnitude and  $B-V$  color from [Prugniel & Heraudeau \(1998\)](#), and the stellar M/L ratio from [Bell & de Jong \(2001\)](#). The contamination from the AGN hosted by NGC 4395 is negligible, yet we conservatively adopt uncertainties of 0.28 mag for the color and 0.2 mag for the magnitude.

Finally, baryonic masses were calculated simply as

$$M_{\text{BARY}} = M_{\text{STARS}} + M_{\text{GAS}} \quad (4)$$

and are reported in Table 6.

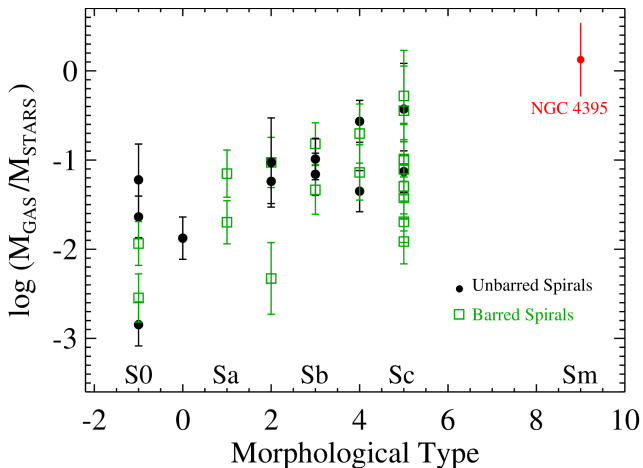


**Figure 6.** Gas fraction as a function of galaxy morphological type. Morphologies are either those listed in NED or from the derived B/T ratios, which were the results of the surface brightness fits carried out by Bentz et al. (2009), Bentz et al. (2013), Bentz et al. (2016), and Bentz & Manne-Nicholas (2018) (see Sec. 4.1, Table 6). Morphologies based on B/T values were assigned according to the mean of the distributions in Figure 6 of Kent (1985). The black circles are unbarred spirals, the green squares are barred spirals.

### 3.4. Black Hole Mass

The parent sample for the galaxies in this study is the reverberation sample of AGNs with direct black hole mass constraints. Reverberation mapping (Blandford & McKee 1982; Peterson 1993) is a light-echo technique in which the radius of the spatially-unresolved broad line region ( $R_{\text{BLR}}$ ) is measured. The BLR of an AGN is composed of optically thick gas moving at large Doppler velocities deep in the potential well of the black hole. The BLR gas is photoionized by the continuum emission source (likely the accretion disk) and gives rise to the characteristic broad emission lines seen in the spectra of Type 1 AGNs. Variations in the continuum flux drive variations in the broad emission line flux, but delayed in time from the observer’s point of view due to the extra path length most of the BLR light must travel to the observer. This time lag value provides a direct measure of the BLR size. Combining  $R_{\text{BLR}}$  and the Doppler-broadened emission line width through the virial theorem yields a constraint on the total mass enclosed within the BLR, the vast majority of which is the mass of the SMBH.

The black hole masses adopted here are from the AGN Black Hole Mass Database (Bentz & Katz 2015), which is a compilation of reverberation-based  $M_{\text{BH}}$  values. Thus, the masses are calculated as

$$M_{\text{BH}} = f \frac{c\tau V^2}{G} \quad (5)$$

where  $c\tau$  is the time delay for a broad emission line,  $V$  is the width of the line, and  $G$  is the gravitational constant. The  $f$  term is an order-unity scaling factor which accounts for the unknown kinematics and geometry of the BLR gas in AGNs. It is generally derived by assuming that the AGN black hole mass - stellar velocity dispersion relationship ( $M_{\text{BH}} - \sigma_{\text{STARS}}$ ; Ferrarese & Merritt 2000; Gebhardt et al. 2000) is the same as that of nearby galaxies with black hole masses from dynamical modeling. We adopt  $\langle f \rangle = 4.3$  which was determined by Grier et al. (2013).

A few of the AGNs in our sample are included in the in-progress updates to the AGN Black Hole Mass Database, and

thus require a little more explanation. For MCG+08-11-011, Mrk 374, and NGC 2617, we employed the virial  $M_{\text{BH}}$  from Fausnaugh et al. (2017), but scaled to match our adopted  $\langle f \rangle$  value. Similarly, we employed the virial  $M_{\text{BH}}$  for Mrk 704 from De Rosa et al. (2018) and rescaled it with our adopted  $\langle f \rangle$  value. For Mrk 1044 and Mrk 493, we utilized the  $H\beta$  time delay ( $\tau_{H\beta}$ ) measurement from Hu et al. (2015) and the width of the  $H\beta$  emission line in the variable, root mean square (rms) spectrum ( $\sigma_{\text{line}}$ ) from Du et al. (2016) together with our adopted  $\langle f \rangle$  value to calculate  $M_{\text{BH}}$ . For NGC 5940 we utilized the  $\sigma_{\text{line}}$  value from Barth et al. (2015) and the  $\tau_{H\beta}$  value from Barth et al. (2013) to determine a black hole mass.

We have adopted a preliminary black hole mass for Mrk 478 based on early analysis of in-hand reverberation-mapping data (de Rosa, private communication). The black hole mass for 1H1934-063 is based on current work on in-hand reverberation-mapping data from Bentz et al. (2019, in prep).

## 4. DISCUSSION

In the past two decades there has been a surge of studies focusing on scaling relationships between host galaxy and SMBH characteristics, and these relationships seem to suggest galaxy – black hole coevolution. Such empirical scaling relations include the relationship between  $M_{\text{BH}}$  and the luminosity of the bulge ( $M_{\text{BH}} - L_{\text{BULGE}}$ ; Kormendy & Richstone 1995), the  $M_{\text{BH}} -$  stellar velocity dispersion relation (Ferrarese & Merritt 2000; Gebhardt et al. 2000), and the most recent calibration of the  $M_{\text{BH}} - M_{\text{STARS}}$  relation found by Bentz & Manne-Nicholas (2018). Many of these scaling relationships are used as inputs or constraints to cosmological galaxy simulations in an attempt to further understand the details of the symbiotic relationship between galaxies and black holes (e.g., Steinborn et al. 2015; Volonteri et al. 2016; Mutlu-Pakdil et al. 2018). Here, we explore potential scaling relationships that include  $M_{\text{GAS}}$ .

Linear regressions were carried out using the Bayesian method-based algorithm LINMIX\_ERR (Kelly 2007), which accounts for measurement uncertainties in both variables and includes an element of random scatter. We report the median and  $1-\sigma$  deviations of large, random samples from the posterior probability distribution as the measurement and uncertainty for the slope, intercept, and scatter of each relationship.

### 4.1. Gas Mass - Stellar Mass Relationship

We first explored the relationship between  $M_{\text{GAS}}$  and  $M_{\text{STARS}}$  in our sample. We might expect to see smaller amounts of gas in galaxies with higher stellar mass if the gas content of these galaxies is not replenished as quickly as it is used up for star formation.

Fig. 5 displays  $M_{\text{STARS}}$  vs.  $M_{\text{GAS}}$ . There is a slight tendency for lower stellar mass to correspond to lower gas mass. The range of stellar and gas masses covered by our sample is fairly small, however, given that most of the points are clumped together at  $9 < \log(M_{\text{GAS}}/M_{\odot}) < 10$  and  $10 < \log(M_{\text{STARS}}/M_{\odot}) < 11$ , and the scatter is quite large.

We next examined whether the fraction of gas-to-stellar content in the galaxies,  $M_{\text{GAS}}/M_{\text{STARS}}$ , might serve as an indicator of morphological type. One might expect the gas content to change as a function of morphology, with lower  $M_{\text{GAS}}$  for early-type spirals, and higher values for later-types.

To explore this, we adopted galaxy morphologies from NED for those galaxies where previous ground-based data provided sufficient angular resolution to determine the morphology (most of the NGC objects, for example). For the

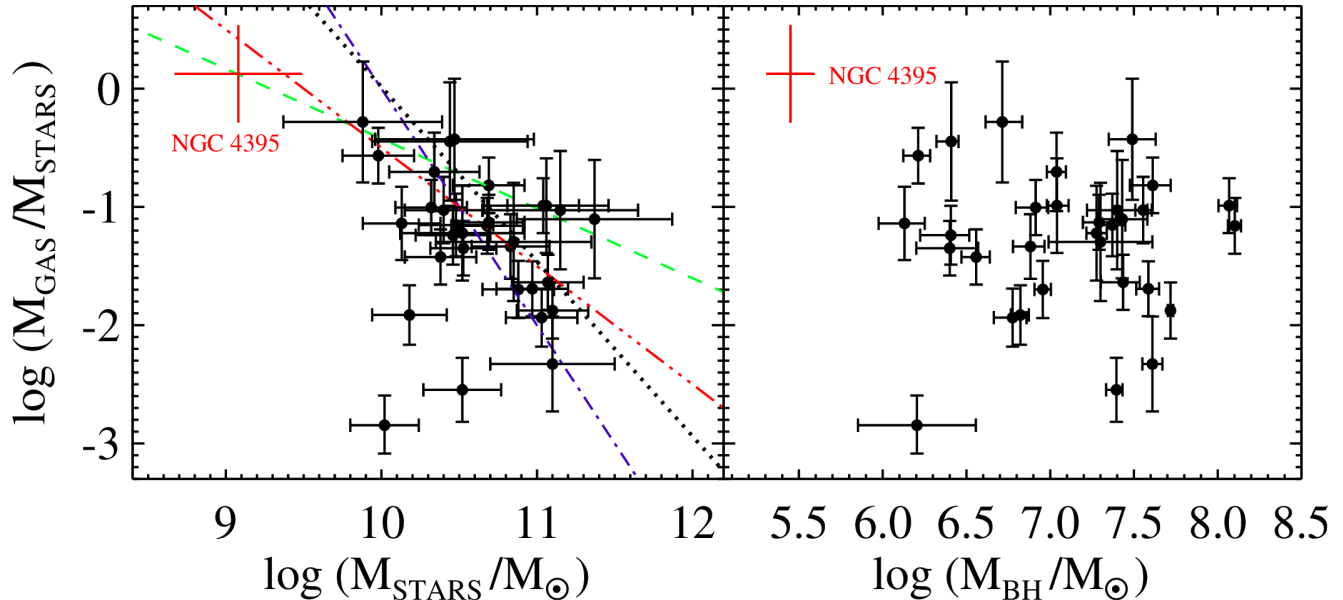


**Figure 7.**  $M_{\text{GAS}}/M_{\text{STARS}}$  as a function of  $M_{\text{STARS}}$  (left) and  $M_{\text{BH}}$  (right). The trend in the left plot shows decreasing mass fraction with increasing values of  $M_{\text{STARS}}$ . The black dotted line is our best fit with a scatter of  $(0.41 \pm 0.24)$  dex. NGC 4395 is not included in the fit. The green dash line is the best-fit line found by [Stewart et al. \(2009\)](#) which characterizes the gas mass fraction of data from [McGaugh \(2005\)](#). The sample used by [Stewart et al. \(2009\)](#) is biased towards gas-rich spirals, while our sample is stellar-rich, which is a possible explanation to the data lying beneath the line. The blue dot-dash line shows a "closed box" relation that demonstrates direct conversion from  $M_{\text{GAS}}$  to  $M_{\text{STARS}}$ . The red dot-dot-dot-dash line shows a constant  $M_{\text{GAS}}$  relation, where  $M_{\text{GAS}}$  remains fixed at the approximate average value of our sample at  $M_{\text{GAS}} \sim 10^{9.5} M_{\odot}$  while  $M_{\text{STARS}}$  varies. On the right plot, there is no evidence of a trend for  $M_{\text{GAS}}/M_{\text{STARS}}$  as a function of  $M_{\text{BH}}$ .

more distant and compact galaxies, we determined the morphological type based on the bulge-to-total (B/T) luminosity ratio as follows. For most of the objects, the surface brightness decompositions of [Bentz et al. \(2009\)](#), [Bentz et al. \(2013\)](#), [Bentz et al. \(2016\)](#), and [Bentz & Manne-Nicholas \(2018\)](#) were used to calculate B/T values, and these were compared to the distributions of B/T relative to galaxy morphology presented by [Kent \(1985\)](#) in their Figure 6. We then adopted the morphology associated with the mean B/T value that most closely matched the B/T measured for each galaxy. For MCG+08-11-011 Mrk 374, NGC 2617, Mrk 704, Mrk 478, NGC 5940, and 1H1934-063, we calculated the B/T ratios from surface brightness decompositions of in-hand HST V-band images. Finally, for Mrk 1044 and Mrk 493, we used the surface brightness decompositions from [Wang et al. \(2014\)](#) in order to derive the B/T ratios.

Fig. 6 shows the gas-to-stellar fraction as a function of morphology. The black circles in Fig. 6 denote unbarred spirals, and the green squares denote barred spirals. The gas-to-stellar fraction appears to be approximately constant as a function of morphology for the barred spirals, albeit with a large scatter and with a lower typical  $M_{\text{GAS}}/M_{\text{STARS}}$  for SB0 galaxies. However the unbarred spirals show a slight preference for a higher gas fraction at later types, especially when the unbarred Sm galaxy NGC 4395 is included.

In addition, we explored the gas-to-stellar fraction as a function of  $M_{\text{STARS}}$ . If the gas reservoir of the galaxy is never refueled by accretion onto the disk, we might expect to see evidence of decreasing gas for galaxies of higher stellar content. However, there would be little evidence of this trend if accretion is ongoing and the reservoir is steadily refueled. In the left panel of Fig. 7 we plot the fraction  $M_{\text{GAS}}/M_{\text{STARS}}$  versus  $M_{\text{STARS}}$  and compare to several simple scenarios. The black dotted line shows the best formal fit to the data points and has

the form

$$\log \frac{M_{\text{GAS}}}{M_{\text{STARS}}} = (-1.48 \pm 1.44) \log \left( \frac{M_{\text{STARS}}}{10^{11} M_{\odot}} \right) - (1.46 \pm 0.14) \quad (6)$$

with a scatter of  $(0.41 \pm 0.24)$  dex. NGC 4395 is not included in our formal fit. The blue dot-dash line represents a "closed-box" relation, where there is a one-to-one correlation between the decrease in  $M_{\text{GAS}}$  and increase in  $M_{\text{STARS}}$ , therefore no cold gas accretion. The slope is slightly steeper than the trend of the data, suggesting that some refueling must be occurring on average for the galaxies in our sample. The red dot-dot-dot-dash line represents a constant  $M_{\text{GAS}}$  relation, where gas is assumed to be replenished at the rate that it is used up for star formation. The slope of this relationship is shallower than our formal fit (which has large uncertainties), suggesting that the average galaxy in this sample is replenishing its gas reservoir, but at a rate that is slower than the gas is being used up. If NGC 4395 is included in the fit, we find a shallower slope of  $(-0.77 \pm 0.42)$ , much closer to that of the constant  $M_{\text{GAS}}$  relation.

[McGaugh \(2005\)](#) compiled a sample of galaxies with extended 21 cm rotation curves and derived gas and stellar masses for an in-depth baryonic Tully-Fisher relation study. [Stewart et al. \(2009\)](#), in their simulation of the baryonic content of galaxy mergers, assigned gas to the simulated galaxies by quantifying the relation between  $M_{\text{GAS}}/M_{\text{STARS}}$  as a function of  $M_{\text{STARS}}$  using the results from [McGaugh \(2005\)](#). Their  $M_{\text{GAS}}/M_{\text{STARS}}$  as a function of  $M_{\text{STARS}}$  at  $z = 0$  is represented by the green dashed line in Fig. 7. The sample from [McGaugh \(2005\)](#) used by [Stewart et al. \(2009\)](#) is biased towards gas-rich galaxies, which explains why their relationship appears to serve as an upper limit to our sample of galaxies. The

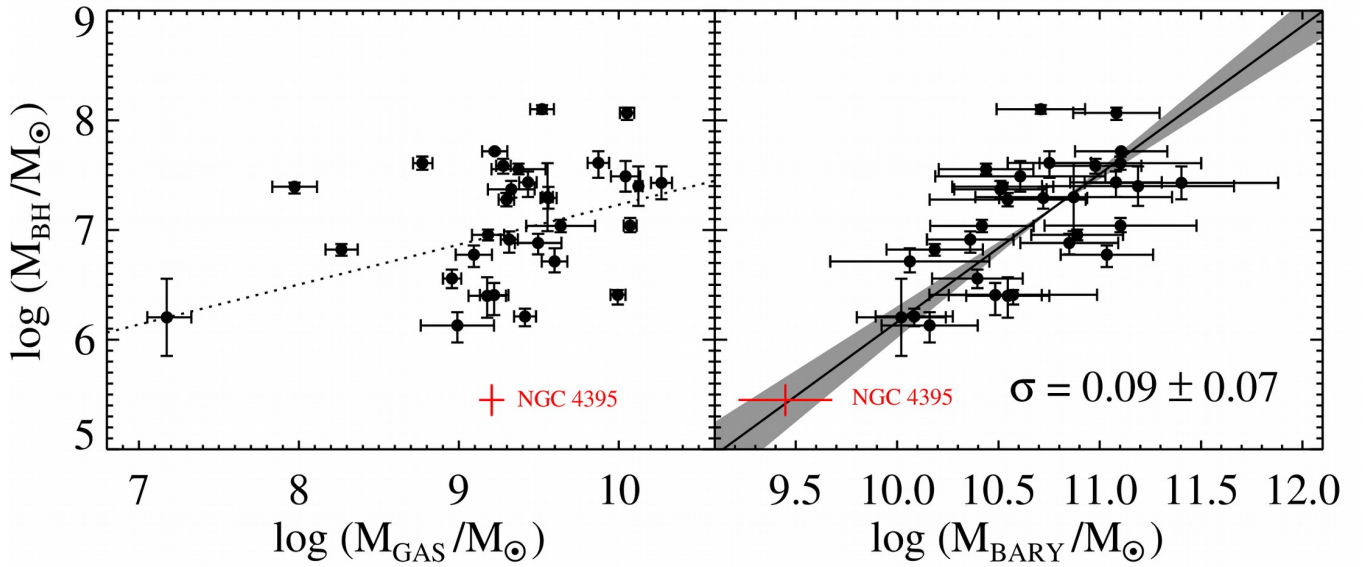


**Figure 8.**  $M_{\text{BH}}$  as a function of  $M_{\text{GAS}}$  (left) and  $M_{\text{BARY}}$  (right). For the data in the left plot, the formal fit for the  $M_{\text{GAS}}-M_{\text{BH}}$  relation includes a scatter of  $(0.32 \pm 0.09)$  dex. On the right, the  $M_{\text{BARY}}-M_{\text{BH}}$  relation seems to exhibit a stronger correlation with less scatter. The red cross in the right panel is a derived baryonic mass for NGC 4395. NGC 4395 is not included in the fit to the black points, nevertheless it seems to follow the same relationship demonstrated by more massive galaxies.

general trend of decreasing gas fraction as  $M_{\text{STARS}}$  increases, however, is consistent between their sample and ours.

A recent study by [Calette et al. \(2018\)](#) included a large sample of early and late-type galaxies from the literature, attempting to homogenize their sample as much as possible, checking against potential biases in the process (i.e., selection effects, upper limits, distances which correct for peculiar motions). They found an overall decrease in  $M_{\text{GAS}}/M_{\text{STARS}}$  as a function of  $M_{\text{STARS}}$  similar to [Stewart et al. \(2009\)](#). However, their average slope from the single- and double-power law best fits is much shallower than ours and the sample of [McGaugh \(2005\)](#). [Bradford et al. \(2015\)](#) conducted a study of the baryonic content of galaxies selected from the Sloan Digital Sky Survey DR8 using isolated HI galaxy detections from the 40% ALFALFA survey ([Haynes et al. 2011](#)), which is a publicly available blind, drift-scan HI survey from the Arecibo Observatory. They also find a decreasing atomic-gas-to-stellar fraction as a function of stellar mass, with a break into a steeper slope at  $M_{\text{STARS}} \approx 10^9 M_{\odot}$ . The slope of the relationship they find after the break is very similar to our best-fit slope.

In addition, we have also explored  $M_{\text{GAS}}/M_{\text{STARS}}$  relative to  $M_{\text{BH}}$ , as shown in the right-hand panel of Fig. 7. We might expect  $M_{\text{STARS}}$  and  $M_{\text{BH}}$  to increase together, since the gas reservoir is used to create stars and fuel the growth of the SMBH. However, we find no evidence for a trend with this sample of AGNs. Instead, our sample demonstrates a relatively constant value of  $M_{\text{GAS}}/M_{\text{STARS}}$  as a function of  $M_{\text{BH}}$ , albeit with a large scatter. A formal fit finds a slope of  $(-0.02 \pm 0.38)$ , which is consistent with zero.

#### 4.2. Gas Mass - Black Hole Mass Relationship

There have been many previous attempts to explore the connection between gas in galaxies and the central supermassive black hole. The vast majority of these studies have focused on AGN characteristics, such as luminosity or accretion rate, instead of the black hole mass itself. Such studies have in-

cluded, for example, exploring correlations between Seyfert nucleus luminosity and HI emission peculiarities ([Heckman et al. 1978](#)), the link between the cold gas reservoir and AGN accretion ([van Gorkom et al. 1989](#); [Peck & Taylor 1998](#)), and the connection between  $M_{\text{HI}}/M_{\text{STARS}}$  and black hole accretion rate ([Fabello et al. 2011](#)). The literature is inconclusive on these themes with other studies finding no evidence of mass transfer from the outer galactic regions to the central AGN when comparing gas content to near-infrared nuclear activity ([Bieging & Biermann 1983](#)) and finding no discernable connection between global gas content and AGN presence ([Ho et al. 2008b](#)). However, even with the myriad of studies that do exist, it appears that no one has yet examined the relationship between gas mass and black hole mass.

The stellar content of galaxies seems to correlate with the black hole mass, for example the  $M_{\text{BH}} - L_{\text{BULGE}}$  ([Kormendy & Richstone 1995](#)),  $M_{\text{BH}} - \sigma_{\text{STARS}}$  ([Ferrarese & Merritt 2000](#)), and  $M_{\text{BH}} - M_{\text{STARS}}$  ([Bentz & Manne-Nicholas 2018](#)) relations. Here we explore whether the gas content also demonstrates a relation to  $M_{\text{BH}}$ .

We plot the reverberation-based black hole masses vs. the gas masses in Fig. 8. There is a weak correlation, with a slight preference for more massive black holes to live in galaxies with larger gas reservoirs, but there is also a large scatter. A formal fit between  $M_{\text{GAS}}$  vs  $M_{\text{BH}}$  finds:

$$\log \frac{M_{\text{BH}}}{M_{\odot}} = (0.36 \pm 0.10) \log \left( \frac{M_{\text{GAS}}}{10^9 M_{\odot}} \right) + (6.87 \pm 0.03) \quad (7)$$

with a scatter of  $(0.32 \pm 0.09)$  dex. We also examined whether morphological type played a role in where objects fell in Fig. 8, but found no obvious trend.

#### 4.3. Baryonic Mass - Black Hole Mass Relationship

[Bentz & Manne-Nicholas \(2018\)](#) recently calibrated the scaling relationship of  $M_{\text{BH}}$  to  $M_{\text{STARS}}$  for the AGN hosts in the reverberation sample. Their best fit based on the M/L

ratio predictions of [Bell & de Jong \(2001\)](#) has a slope of  $(1.69 \pm 0.46)$  and an intercept of  $(8.05 \pm 0.18)$ , with a scatter of  $(0.38 \pm 0.13)$  dex. In the right panel of [Fig. 8](#), we show the relationship between  $M_{\text{BH}}$  and total baryonic masses for galaxies in our sample, many of which were included in the study by [Bentz & Manne-Nicholas \(2018\)](#). The best fit is given by:

$$\log \frac{M_{\text{BH}}}{M_{\odot}} = (1.35 \pm 0.18) \log \left( \frac{M_{\text{BARY}}}{10^{11} M_{\odot}} \right) + (7.51 \pm 0.04) \quad (8)$$

with a scatter of  $(0.09 \pm 0.07)$  dex. The fits to both  $M_{\text{BH}} - M_{\text{BARY}}$  and  $M_{\text{BH}} - M_{\text{STARS}}$  are normalized at  $10^{11} M_{\odot}$ , allowing for easier comparison. The stellar content accounts for the majority of the baryonic mass in these galaxies, so the slopes of the two relationships are formally indistinguishable. The typical fraction of  $M_{\text{GAS}}/M_{\text{STARS}}$  is about 10% for these galaxies, but reaches as high as 52% for Mrk 1044 and 134% for NGC 4395. The slight increase in baryonic mass over stellar mass accounts for the 0.5 dex shift in the intercept between the two relationships.

Interestingly, even though NGC 4395 has a significantly larger  $M_{\text{GAS}}/M_{\text{STARS}}$  than any of the other galaxies in our sample, it appears to follow the same relationship between black hole mass and baryonic mass as the other galaxies in our sample. NGC 4395 is not included in our fit to the rest of the data, but if we include it, we find a very similar slope of  $(1.34 \pm 0.09)$ . This initial study suggests that the SMBHs of AGNs are not only correlated to their stellar content, but the total baryonic mass.

## 5. SUMMARY

We present results from HI spectroscopy of 44 AGNs with reverberation-mapped black hole masses. We detect HI 21 cm emission in 31 of them, 12 of which are the first reported 21 cm detections. Measurements of the integrated HI fluxes,  $W_{50}$ ,  $W_{20}$ , and  $V_{\text{R}}$  values are determined with two independent methods and are found to be generally consistent. From the HI fluxes, we determine  $M_{\text{GAS}}$  for each galaxy. Using the stellar masses provided by [Bentz & Manne-Nicholas \(2018\)](#) as well as derived  $M_{\text{STARS}}$  values from in-hand data and the literature, we also produce total  $M_{\text{BARY}}$  values for the galaxies in our sample.

We have explored a number of relationships involving  $M_{\text{GAS}}$ . We find no evidence for a correlation between  $M_{\text{STARS}}$  and  $M_{\text{GAS}}$ . We find a weak correlation between  $M_{\text{BH}}$  and  $M_{\text{GAS}}$ , albeit with a large scatter, and with no obvious trends based on morphological type. We find that the typical  $M_{\text{GAS}}/M_{\text{STARS}}$  value for our sample is  $\sim 10\%$ . For unbarred spirals, there is a slight preference for later morphological types to have larger  $M_{\text{GAS}}/M_{\text{STARS}}$ . For barred spirals, on the other hand, the gas fraction appears to be mostly constant as a function of morphology except for SB0 galaxies, where  $M_{\text{GAS}}/M_{\text{STARS}}$  is decidedly lower.

We find evidence of a trend of decreasing  $M_{\text{GAS}}/M_{\text{STARS}}$  as a function of  $M_{\text{STARS}}$ , consistent with findings by other groups, yet we detect no trend with  $M_{\text{GAS}}/M_{\text{STARS}}$  as a function of  $M_{\text{BH}}$ . Finally, we find a significant correlation between  $M_{\text{BH}}$  vs  $M_{\text{BARY}}$ , with similar slope to the recalibrated  $M_{\text{BH}} - M_{\text{STARS}}$  relation by [Bentz & Manne-Nicholas \(2018\)](#). The dwarf Seyfert NGC 4395 (which hosts the lowest reverberation-mapped black hole mass) is significantly more gas dominated than the other galaxies in our study, with  $M_{\text{GAS}}/M_{\text{STARS}} = 134\%$ , but it appears to follow the same trend in  $M_{\text{BH}}$  vs  $M_{\text{BARY}}$  defined by the other galaxies in our sample.

We thank the referee for helpful suggestions that improved the clarity of this paper. We thank Joy Skipper for helpful comments on observing scripts and data reduction.

M.C.B gratefully acknowledges support from the NSF through CAREER grant AST-1253702.

H.M.C. acknowledges support by the CNES and Institut Universitaire de France.

This research has made use of the NASA/IPAC Extragalactic Database (NED), which is operated by the Jet Propulsion Laboratory, California Institute of Technology, under contract with the National Aeronautics and Space Administration.

## REFERENCES

- Arakelian, M. A., Dibay, E. A., Yesipov, V. F., & Markarian, B. E. 1971, *Astrofizika*, 7, 177
- Argudo-Fernández, M., Verley, S., Bergond, G., et al. 2015, *A&A*, 578, A110
- Athanassoula, E. 2008, *MNRAS*, 390, L69
- Barth, A. J., Pancoast, A., Bennert, V. N., et al. 2013, *ApJ*, 769, 128
- Barth, A. J., Bennert, V. N., Canalizo, G., et al. 2015, *ApJS*, 217, 26
- Bell, E. F., & de Jong, R. S. 2001, *ApJ*, 550, 212
- Bennett, C. L., Larson, D., Weiland, J. L., & Hinshaw, G. 2014, *ApJ*, 794, 135
- Bentz, M. C., Cackett, E. M., Crenshaw, D. M., et al. 2016, *ApJ*, 830, 136
- Bentz, M. C., & Katz, S. 2015, *PASP*, 127, 67
- Bentz, M. C., & Manne-Nicholas, E. 2018, *ApJ*, 864, 146
- Bentz, M. C., Peterson, B. M., Netzer, H., Pogge, R. W., & Vestergaard, M. 2009, *ApJ*, 697, 160
- Bentz, M. C., Denney, K. D., Grier, C. J., et al. 2013, *ApJ*, 767, 149
- Bieging, J. H., & Biermann, P. 1983, *AJ*, 88, 161
- Biermann, P., Clarke, J. N., & Fricke, K. J. 1979, *A&A*, 75, 19
- Bigiel, F., Leroy, A., Walter, F., et al. 2008, *AJ*, 136, 2846
- Blandford, R. D., & McKee, C. F. 1982, *ApJ*, 255, 419
- Bournaud, F., Elmegreen, B. G., Teyssier, R., Block, D. L., & Puerari, I. 2010, *MNRAS*, 409, 1088
- Bradford, J. D., Geha, M. C., & Blanton, M. R. 2015, *ApJ*, 809, 146
- Buta, R., Mitra, S., de Vaucouleurs, G., & Corwin, Jr., H. G. 1994, *AJ*, 107, 118
- Calette, A. R., Avila-Reese, V., Rodríguez-Puebla, A., Hernández-Toledo, H., & Papastergis, E. 2018, submitted
- Cortese, L., Catinella, B., & Janowiecki, S. 2017, *ApJL*, 848, L7
- Courtois, H. M., Tully, R. B., Fisher, J. R., et al. 2009, *AJ*, 138, 1938
- Cox, A. N. 2000, *Allen's astrophysical quantities*
- Davis, L. E., & Seaquist, E. R. 1983, *ApJS*, 53, 269
- Davoust, E., & Contini, T. 2004, *A&A*, 416, 515
- De Rosa, G., Fausnaugh, M. M., Grier, C. J., et al. 2018, *ApJ*, 866, 133
- de Vaucouleurs, G., de Vaucouleurs, A., Corwin, Jr., H. G., et al. 1991, *S&T*, 82, 621
- de Vaucouleurs, G., de Vaucouleurs, A., & Corwin, J. R. 1976, in *Second reference catalogue of bright galaxies*, Vol. 1976, p. Austin: University of Texas Press., Vol. 1976
- Dekel, A., Sari, R., & Ceverino, D. 2009, *ApJ*, 703, 785
- Dickel, J. R., & Rood, H. J. 1978, *ApJ*, 223, 391
- Doyle, M. T., Drinkwater, M. J., Rohde, D. J., et al. 2005, *MNRAS*, 361, 34
- Du, P., Lu, K.-X., Zhang, Z.-X., et al. 2016, *VizieR Online Data Catalog*, 182
- Elmegreen, B. G., Bournaud, F., & Elmegreen, D. M. 2008, *ApJ*, 688, 67
- Epstein, E. E. 1964, *AJ*, 69, 490
- Fabello, S., Kauffmann, G., Catinella, B., et al. 2011, *MNRAS*, 416, 1739
- Falco, E. E., Kurtz, M. J., Geller, M. J., et al. 1999, *PASP*, 111, 438
- Fausnaugh, M. M., Grier, C. J., Bentz, M. C., et al. 2017, *ApJ*, 840, 97
- Ferrarese, L., & Merritt, D. 2000, *ApJL*, 539, L9
- Fisher, J. R., & Tully, R. B. 1977, *Comments on Astrophysics*, 7, 85
- . 1981, *ApJS*, 47, 139
- Fisher, K. B., Huchra, J. P., Strauss, M. A., et al. 1995, *ApJS*, 100, 69
- Fouque, P., Gourgoulhon, E., Chamaraux, P., & Paturel, G. 1992, *A&AS*, 93, 211
- Freedman, W. L., Madore, B. F., Gibson, B. K., et al. 2001, *ApJ*, 553, 47
- Gallimore, J. F., Baum, S. A., O'Dea, C. P., Pedlar, A., & Brinks, E. 1999, *ApJ*, 524, 684
- Gebhardt, K., Bender, R., Bower, G., et al. 2000, *ApJL*, 539, L13
- Genzel, R., Förster Schreiber, N. M., Lang, P., et al. 2014, *ApJ*, 785, 75
- Giovanelli, R., Haynes, M. P., Kent, B. R., et al. 2005, *AJ*, 130, 2598

- Granato, G. L., Zitelli, V., Bonoli, F., et al. 1993, *ApJS*, 89, 35
- Grier, C. J., Martini, P., Watson, L. C., et al. 2013, *ApJ*, 773, 90
- Hakobyan, A. A., Adibekyan, V. Z., Aramyan, L. S., et al. 2012, *A&A*, 544, A81
- Hann, J. v. 1903, New York, The Macmillan company, 1
- Haynes, M. P., & Giovanelli, R. 1984, *AJ*, 89, 758
- Haynes, M. P., Giovanelli, R., Martin, A. M., et al. 2011, *AJ*, 142, 170
- . 2013, *VizieR Online Data Catalog*, J/AJ/142/170
- Heckman, T. M., Balick, B., & Sullivan, III, W. T. 1978, *ApJ*, 224, 745
- Heckman, T. M., & Best, P. N. 2014, *ARA&A*, 52, 589
- Hernán Caballero, A. 2012, *MNRAS*, 427, 816
- Ho, L. C., Darling, J., & Greene, J. E. 2008a, *ApJS*, 177, 103
- . 2008b, *ApJ*, 681, 128
- Ho, L. C., & Kim, M. 2009, *The Astrophysical Journal Supplement Series*, 184, 398
- Hu, C., Du, P., Lu, K.-X., et al. 2015, *ApJ*, 804, 138
- Huchra, J., Latham, D. W., da Costa, L. N., Pellegrini, P. S., & Willmer, C. N. A. 1993, *AJ*, 105, 1637
- Huchtmeier, W. K., & Richter, O.-G. 1989, *A General Catalog of HI Observations of Galaxies. The Reference Catalog.*, 350
- Humason, M. L., Mayall, N. U., & Sandage, A. R. 1956, *AJ*, 61, 97
- Hutchings, J. B. 1989, *AJ*, 98, 524
- Joshi, R., Chand, H., Wiita, P. J., Gupta, A. C., & Srikanand, R. 2012, *MNRAS*, 419, 3433
- Kaldare, R., Colless, M., Raychaudhury, S., & Peterson, B. A. 2003, *MNRAS*, 339, 652
- Keel, W. C. 1996, *AJ*, 111, 696
- Kelly, B. C. 2007, *ApJ*, 665, 1489
- Kent, S. M. 1985, *ApJS*, 59, 115
- König, S., Eckart, A., García-Marín, M., & Huchtmeier, W. K. 2009, *A&A*, 507, 757
- Koribalski, B. S., Staveley-Smith, L., Kilborn, V. A., et al. 2004, *AJ*, 128, 16
- Kormendy, J., & Ho, L. C. 2013, *ARA&A*, 51, 511
- Kormendy, J., & Kennicutt, R. C. 2004, *Annual Review of Astronomy and Astrophysics*, 42, 603
- Kormendy, J., & Richstone, D. 1995, *ARA&A*, 33, 581
- Leroy, A. K., Walter, F., Brinks, E., et al. 2008, *AJ*, 136, 2782
- Lewis, B. M. 1983, *AJ*, 88, 1695
- . 1987, *The Astrophysical Journal Supplement Series*, 63, 515
- Liszt, H. S., & Dickey, J. M. 1995, *AJ*, 110, 998
- MacKenty, J. W. 1990, *ApJS*, 72, 231
- Marganian, P., Garwood, R. W., Braatz, J. A., Radziwill, N. M., & Maddalena, R. J. 2006, in *Astronomical Society of the Pacific Conference Series*, Vol. 351, *Astronomical Data Analysis Software and Systems XV*, ed. C. Gabriel, C. Arviset, D. Ponz, & S. Enrique, 512
- Martin, C. L., & Kennicutt, Jr., R. C. 2001, *ApJ*, 555, 301
- Martin, M. C. 1998, *Astronomy and Astrophysics Supplement Series*, 131, 73
- Martini, P. 2004, in *IAU Symposium*, Vol. 222, *The Interplay Among Black Holes, Stars and ISM in Galactic Nuclei*, ed. T. Storchi-Bergmann, L. C. Ho, & H. R. Schmitt, 235–241
- Maza, J., & Ruiz, M. T. 1989, *The Astrophysical Journal Supplement Series*, 69, 353
- McGaugh, S. S. 2005, *ApJ*, 632, 859
- . 2012, *AJ*, 143, 40
- McGaugh, S. S., & de Blok, W. J. G. 1997, *ApJ*, 481, 689
- McMahon, R. G., Banerji, M., Gonzalez, E., et al. 2013, *The Messenger*, 154, 35
- Mendoza-Castrejón, S., Dultzin, D., Krongold, Y., González, J. J., & Elitzur, M. 2015, *MNRAS*, 447, 2437
- Meyer, M. J., Zwaan, M. A., Webster, R. L., et al. 2004, *MNRAS*, 350, 1195
- Mirabel, I. F., & Sanders, D. B. 1988, *ApJ*, 335, 104
- Mirabel, I. F., & Wilson, A. S. 1984, *ApJ*, 277, 92
- Monroe, T. R., Prochaska, J. X., Tejos, N., et al. 2016, *AJ*, 152, 25
- Mundell, C., Pedlar, A., G., et al. 1995, *Monthly Notices of the Royal Astronomical Society*, 277, 641
- Mutlu-Pakdil, B., Seigar, M. S., Hewitt, I. B., et al. 2018, *MNRAS*, 474, 2594
- Obreschkow, D., & Rawlings, S. 2009, *MNRAS*, 394, 1857
- Oh, K., Yi, S. K., Schawinski, K., et al. 2015, *The Astrophysical Journal Supplement Series*, 219, 1
- Osterbrock, D. E., & Pogge, R. W. 1987, *ApJ*, 323, 108
- Panessa, F., de Rosa, A., Bassani, L., et al. 2011, *MNRAS*, 417, 2426
- Patrel, G., Theureau, G., Bottinelli, L., et al. 2003, *A&A*, 412, 57
- Payne, C. H. 1925, PhD thesis, RADCLIFFE COLLEGE.
- Peck, A. B., & Taylor, G. B. 1998, *ApJL*, 502, L23
- Pedlar, A., Howley, P., Axon, D. J., & Unger, S. W. 1992, *MNRAS*, 259, 369
- Peterson, B. M. 1993, *PASP*, 105, 247
- Peterson, S. D. 1979, *ApJS*, 40, 527
- Proust, D., Mazure, A., Vandierriest, C., Sodre, L., J., & Capelato, H. V. 1995, *Astronomy and Astrophysics Supplement Series*, 114, 565
- Prugniel, P., & Heraudeau, P. 1998, *A&AS*, 128, 299
- Ramella, M., Geller, M. J., Huchra, J. P., & Thorstensen, J. R. 1995, *AJ*, 109, 1458
- Reyes, R., Mandelbaum, R., Gunn, J. E., Pizagno, J., & Lackner, C. N. 2011, *MNRAS*, 417, 2347
- Richards, G. T., Myers, A. D., Gray, A. G., et al. 2009, *The Astrophysical Journal Supplement Series*, 180, 67
- Richter, O.-G., & Huchtmeier, W. K. 1982, *A&A*, 109, 155
- Rieke, G. H. 1978, *ApJ*, 226, 550
- Riffel, R., Rodríguez-Ardila, A., Aleman, I., et al. 2013, *MNRAS*, 430, 2002
- Rines, K., Geller, M. J., Diaferio, A., Mohr, J. J., & Wegner, G. A. 2000, *AJ*, 120, 2338
- Rines, K. J., Geller, M. J., Diaferio, A., & Hwang, H. S. 2016, *ApJ*, 819, 63
- Roberts, M. S. 1962, *AJ*, 67, 437
- . 1969, *AJ*, 74, 859
- Shi, Y., Rieke, G. H., Ogle, P. M., Su, K. Y. L., & Balog, Z. 2014, *The Astrophysical Journal Supplement Series*, 214, 23
- Shostak, G. S. 1978, *A&A*, 68, 321
- Smith, B. J., Kleinmann, S. G., Huchra, J. P., & Low, F. J. 1987, *ApJ*, 318, 161
- Smith, K. L., Boyd, P. T., Mushotzky, R. F., et al. 2015, *AJ*, 150, 126
- Steinborn, L. K., Dolag, K., Hirschmann, M., Prieto, M. A., & Remus, R.-S. 2015, *MNRAS*, 448, 1504
- Stewart, K. R., Bullock, J. S., Wechsler, R. H., & Maller, A. H. 2009, *ApJ*, 702, 307
- Stierwalt, S., Haynes, M. P., Giovanelli, R., et al. 2005, in *Bulletin of the American Astronomical Society*, Vol. 37, *American Astronomical Society Meeting Abstracts*, 1480
- Stocke, J. T., Morris, S. L., Gioia, I. M., et al. 1991, *The Astrophysical Journal Supplement Series*, 76, 813
- Strauss, M. A., & Huchra, J. 1988, *AJ*, 95, 1602
- Strauss, M. A., Huchra, J. P., Davis, M., et al. 1992, *The Astrophysical Journal Supplement Series*, 83, 29
- Teng, S. H., Veilleux, S., & Baker, A. J. 2013, *ApJ*, 765, 95
- Theureau, G., Bottinelli, L., Coudreau-Durand, N., et al. 1998, *A&AS*, 130, 333
- Theureau, G., Hanski, M., Coudreau, N., Hallet, N., & Martin, J.-M. 2006, *VizieR Online Data Catalog*, 346
- Theureau, G., Coudreau, N., Hallet, N., et al. 2005, *A&A*, 430, 373
- Thim, F., Hoessel, J. G., Saha, A., et al. 2004, *AJ*, 127, 2322
- Tift, W. G., & Cocke, W. J. 1988, *The Astrophysical Journal Supplement Series*, 67, 1
- Tilton, E. M., Danforth, C. W., Shull, J. M., & Ross, T. L. 2012, *ApJ*, 759, 112
- Tonry, J. L., Dressler, A., Blakeslee, J. P., et al. 2001, *ApJ*, 546, 681
- Tully, R. B., & Fisher, J. R. 1977, *A&A*, 54, 661
- Tully, R. B., Rizzi, L., Shaya, E. J., et al. 2009a, *AJ*, 138, 323
- . 2009b, *AJ*, 138, 323
- Tully, R. B., Shaya, E. J., Karachentsev, I. D., et al. 2008, *ApJ*, 676, 184
- Tyson, J. A., Fischer, P., Guhathakurta, P., et al. 1998, *AJ*, 116, 102
- van Driel, W., Marcum, P., Gallagher, III, J. S., et al. 2001, *A&A*, 378, 370
- van Gorkom, J. H., Knapp, G. R., Ekers, R. D., et al. 1989, *AJ*, 97, 708
- Verheijen, M. A. W., & Sancisi, R. 2001, *A&A*, 370, 765
- Volonteri, M., Dubois, Y., Pichon, C., & Devriendt, J. 2016, *MNRAS*, 460, 2979
- Wang, J.-M., Du, P., Hu, C., et al. 2014, *ApJ*, 793, 108
- Westmeier, T., Jurek, R., Obreschkow, D., Koribalski, B. S., & Staveley-Smith, L. 2014, *MNRAS*, 438, 1176
- Wolfinger, K., Kilborn, V. A., Koribalski, B. S., et al. 2013, *MNRAS*, 428, 1790
- Wong, D. S., Chornock, R., & Filippenko, A. V. 2008, *Publications of the Astronomical Society of the Pacific*, 120, 266
- Wong, T., & Blitz, L. 2002, *ApJ*, 569, 157
- Wu, X.-B., & Jia, Z. 2010, *MNRAS*, 406, 1583
- Young, J. S., & Knezek, P. M. 1989, *ApJL*, 347, L55



**Table 1**  
Target Observations

Target	RA (hh mm ss.s)	Dec (dd mm ss)	$z$	Session Number	Scans	Date (yyyy-mm-dd)	UT (hh mm ss)	LST (hh:mm:ss)	Hour Angle	Backend
(1)	(2)	(3)	(4)	(5)	(6)	(7)	(8)	(9)	(10)	(11)
Mrk 1501	00 10 31.0	+10 58 30	0.08934	2	6-52	2013-02-05	22 57 55.0	02 43 24.8	2.90	G
				4	6-162	2013-02-08	21 14 15.0	02 11 00.5	1.01	G
				9	6-23	2013-02-15	18 06 40.0	22 30 56.7	-1.64	G
				54	6-43	2013-06-30	09 07 41.0	22 22 31.8	-1.74	G
				55	6-33	2013-07-01	09 52 59.0	23 11 57.8	-0.92	G
				62	6-19	2013-08-10	05 53 18.0	21 49 25.4	-2.31	G
				64	6-22	2013-08-12	05 16 04.0	21 19 57.3	-2.83	G
Mrk 1044	02 30 05.5	-08 59 53	0.01645	38	6-132	2018-09-06	09 06 28.5	02 48 47.0	0.31	V
3C120	04 33 11.1	+05 21 16	0.03301	44	6-139	2018-09-16	06 59 59.5	01 21 22.7	-1.15	V
				20	7-106	2013-03-13	01 37 35.0	06 45 10.8	2.21	G
Ark 120	05 16 11.4	-00 08 66	0.03271	23	6-90	2013-03-27	23 10 33.0	06 13 09.1	1.67	G
				27	1-52	2013-04-03	21 28 57.0	04 58 58.4	0.44	G
				59	6-25	2013-07-27	18 18 09.0	09 21 04.7	4.83	G
				65	6-20	2013-08-30	17 19 56.0	10 36 46.1	-8.01	G
				69	6-96	2013-09-03	11 16 53.0	04 48 00.1	0.26	G
MCG+08-11-011	05 54 53.6	+46 26 22	0.02048	45	146-277	2018-09-16	12 38 53.5	07 01 12.4	1.75	V
				52	6-135	2018-10-16	09 20 48.5	05 40 51.4	0.41	V
Mrk 6	06 52 12.2	+74 25 37	0.01881	46	6-135	2018-09-20	08 15 37.5	02 52 59.3	-3.03	V
				53	6-129	2018-10-17	09 19 05.5	05 43 04.7	-0.20	V
Mrk 374	06 59 38.1	+54 11 48	0.04263	6	6-105	2013-02-26	02 26 11.0	07 34 35.3	1.88	G
				10	6-91	2013-02-21	04 36 55.0	09 22 25.2	2.52	G
				12	6-48	2013-02-26	23 09 41.0	04 18 05.3	-2.53	G
Mrk 79	07 42 32.8	+49 48 35	0.02219	32	6-137	2018-09-01	09 22 29.5	02 45 07.8	-4.24	V
				35	6-84	2018-09-04	16 52 10.5	10 27 52.4	3.47	V
				36	6-50	2018-09-05	11 05 51.5	04 44 33.0	-2.25	V
NGC 2617	08 35 38.8	-04 05 18	0.01421	3	32-53	2013-02-07	06 33 43.0	10 24 32.6	2.72	G
				51	6-133	2018-10-15	12 23 45.5	08 40 21.9	0.08	V
Mrk 704	09 18 26.0	+16 18 19	0.02923	55	6-135	2018-10-25	13 22 04.5	10 18 16.0	1.71	V
				37	56-181	2018-09-05	14 47 00.5	08 26 18.3	-0.87	V
				49	6-135	2018-10-14	12 13 26.5	08 26 04.6	-0.87	V
				68	8-135	2019-01-02	05 18 08.5	06 45 02.8	-2.56	V
Mrk 110	09 25 12.9	+52 17 11	0.03529	71	6-59	2019-01-08	08 51 54.5	10 43 03.3	1.27	V
				31	142-275	2018-08-31	11 17 01.5	04 36 02.1	-4.82	V
				33	143-270	2018-09-01	14 42 26.5	08 05 57.4	-1.32	V
NGC 3227	10 23 30.6	+19 51 54	0.00386	8	6-13	2013-02-15	05 56 56.0	10 19 14.6	-0.05	G
Mrk 142	10 25 31.3	+51 40 36	0.04494	5	6-147	2013-02-09	04 00 06.0	11 55 48.0	0.27	G
NGC 3516	11 06 47.5	+72 34 07	0.00884	11	6-91	2013-02-23	06 16 32.0	11 10 10.6	0.83	G
				3	22-31	2013-02-07	05 53 49.0	09 44 34.4	-1.35	G
				53	6-76	2013-06-24	02 08 21.0	14 58 25.5	3.87	G
				41	6-137	2018-09-09	02 36 23.5	20 29 27.6	9.38	V
				43	142-274	2018-09-11	02 48 40.5	20 49 39.7	9.71	V
				61	6-119	2018-12-21	02 15 07.5	02 54 13.1	-8.65	V
				62	6-75	2018-12-21	07 35 51.5	08 15 49.7	-3.29	V
				63	6-161	2018-12-22	00 07 18.5	00 49 59.6	-10.28	V
				64	6-81	2018-12-22	21 28 52.5	22 15 04.2	11.14	V
				65-66	6-138	2019-01-01	01 19 46.5	02 42 05.1	-8.86	V
				69	6-99	2019-01-03	23 34 38.5	01 08 29.5	-10.42	V
SBS 1116+583A	11 18 57.7	+58 03 24	0.02787	70	6-73	2019-01-05	22 07 14.5	23 48 44.3	-11.30	V
				72	7-32	2019-01-08	10 41 31.5	12 32 58.3	0.99	V
				29	6-84	2013-04-05	01 46 15.0	08 24 36.5	-2.91	G
				36	6-93	2013-05-06	22 28 41.0	08 08 51.4	-3.15	G
				39	6-69	2013-05-09	21 26 51.0	07 18 47.8	-3.74	G
				31	66-243	2013-04-30	04 02 57.0	13 16 01.1	1.85	G
				50	6-76	2013-06-01	01 07 14.0	11 30 14.5	-1.47	G
NGC 4051	12 03 09.6	+44 31 53	0.00234	50	6-284	2018-08-16	09 54 44.5	02 14 23.3	-9.52	V
Arp 151	11 25 36.2	+54 22 57	0.02109	29	26-98	2013-07-27	20 50 37.0	11 53 52.0	-1.48	G
				60	36-96	2013-07-29	01 40 05.0	16 39 50.4	3.04	G
				3	6-13	2013-02-07	05 18 08.0	09 18 48.4	-2.98	G
				46	36-119	2013-05-23	00 15 46.0	10 59 19.0	-2.72	G
				47	6-95	2013-05-25	23 36 13.0	10 31 28.2	-3.29	G
NGC 4151	12 10 32.6	+39 24 19	0.00332	49	2270-2352	2013-05-27	23 52 16.0	10 55 28.1	-2.78	G
				3	14-21	2013-02-07	05 33 14.0	09 23 57.6	-2.78	G
				45	6-241	2013-05-22	01 52 39.0	12 32 47.8	0.24	G
				49	2240-2269	2013-05-27	21 36 54.0	08 40 00.1	-3.64	G
NGC 4253	12 18 26.5	+29 48 46	0.01293	47	6-109	2018-09-25	12 18 27.3	09 20 27.3	-2.97	V
				48	6-133	2018-10-12	14 51 38.5	10 56 49.5	-1.44	V
Mrk 50	12 23 24.1	+02 40 45	0.02343	50	142-271	2018-10-14	17 51 50.5	14 05 24.2	1.70	V
PG 1229+204	12 32 03.6	+20 09 28	0.06301	17	6-15	2013-03-05	03 59 27.0	09 32 25.6	-2.99	G
				42	6-81	2013-05-19	00 52 09.0	11 20 18.2	-1.20	G
				43	6-99	2013-05-20	03 06 54.0	13 39 21.9	1.12	G
				46	6-35	2013-05-22	22 00 35.0	08 44 02.2	-3.80	G
NGC 4593	12 39 39.4	-05 20 39	0.00900	38	6-77	2013-05-09	03 06 56.0	12 56 01.8	0.27	G
				41	6-116	2013-05-18	01 07 31.0	11 31 46.1	-1.13	G
NGC 4748	12 52 12.4	-13 24 53	0.01463	7	6-87	2013-02-14	07 27 03.0	11 45 41.2	-1.11	G

**Table 1**  
Target Observations

Target	RA (hh mm ss.s)	Dec (dd mm ss)	$z$	Session Number	Scans	Date (yyyy-mm-dd)	UT (hh mm ss)	LST (hh:mm:ss)	Hour Angle	Backend
(1)	(2)	(3)	(4)	(5)	(6)	(7)	(8)	(9)	(10)	(11)
				37	10-93	2013-05-08	03 56 07.0	13 41 24.3	0.82	G
				44	6-36	2013-05-21	01 21 09.0	11 57 16.0	-0.92	G
				47	96-147	2013-05-26	02 29 44.0	13 25 45.1	0.56	G
MCG-06-30-015	13 35 53.7	-34 17 44	0.00775	8	14-27	2013-02-15	06 27 25.0	10 49 49.9	-2.77	G
				59	99-151	2013-07-27	23 13 36.0	14 17 27.9	0.69	G
				60	6-35	2013-07-28	23 19 44.0	14 27 33.5	0.86	G
				61	6-117	2013-08-03	22 35 46.0	14 07 07.6	0.52	G
MCG-05-33-019	13 49 19.2	-30 18 34	0.01514	24	6-86	2013-04-01	07 19 54.0	14 39 52.3	0.84	G
				30	6-87	2013-04-29	05 24 26.0	14 34 28.8	0.79	G
				48	6-69	2013-05-27	01 59 39.0	12 59 31.7	-0.83	G
Mrk 279	13 53 03.4	+69 18 31	0.03045	13	31-82	2013-03-01	00 55 27.0	06 12 09.1	-7.68	G
				14	6-99	2013-03-02	23 49 04.0	05 13 28.3	-8.66	G
				22	6-75	2013-03-24	12 08 09.0	18 57 22.3	5.07	G
				25	6-64	2013-04-01	10 24 57.0	17 45 25.7	3.87	G
				31	6-65	2013-04-29	10 34 25.0	19 45 18.7	5.87	G
NGC 5548	14 17 59.5	+25 08 12	0.01718	28	6-102	2013-04-04	09 46 21.0	17 18 33.1	3.01	G
				33	6-75	2013-05-01	07 38 06.0	16 56 23.9	2.64	G
				37	94-161	2013-05-08	06 55 11.0	16 40 57.7	2.38	G
PG 1426+015	14 29 06.6	+01 17 06	0.08657	58	6-133	2018-11-26	13 52 30.5	12 54 56.7	-1.57	V
				59	6-133	2018-11-27	16 24 05.5	15 30 53.2	1.03	V
				67	6-123	2019-01-01	14 37 48.5	16 02 18.2	1.42	V
Mrk 817	14 36 22.1	+58 47 39	0.03146	32	7-113	2013-04-30	09 56 12.0	19 10 56.0	4.58	G
				35	7-66	2013-05-06	10 06 48.0	19 45 13.1	5.15	G
				40	6-98	2013-05-11	07 41 23.0	17 39 06.9	3.05	G
				56	9-54	2013-07-07	18 22 10.0	08 06 22.9	-6.50	G
Mrk 478	14 42 07.5	+35 26 23	0.07906	42	6-135	2018-09-10	21 23 08.5	15 23 14.2	0.69	V
				54	6-139	2018-10-17	14 48 36.5	11 13 29.8	-3.48	V
NGC 5940	15 31 18.1	+07 27 28	0.03393	57	6-137	2018-11-07	20 06 12.5	17 54 45.6	2.39	V
				60	6-135	2018-11-28	15 17 07.5	14 27 40.7	-1.06	V
Mrk 290	15 35 52.3	+57 54 09	0.02958	1	6-177	2013-02-05	13 44 31.0	17 28 42.2	1.88	G
				17	16-51	2013-03-05	04 54 53.0	10 28 00.7	-5.13	G
Mrk 493	15 59 09.6	+35 01 47	0.03133	34	6-131	2018-09-02	20 54 26.5	14 22 55.0	-1.60	V
				56	6-139	2018-10-30	14 48 53.5	12 05 02.0	-3.90	V
3C390.3	18 42 09.0	+79 46 17	0.05610	13	6-25	2013-02-28	23 15 04.0	04 31 29.6	9.82	G
				26	6-64	2013-04-01	11 30 26.0	18 58 58.6	0.28	G
				52	6-70	2013-06-23	13 39 28.0	02 27 42.7	7.76	G
				60	97-108	2013-07-29	03 29 26.0	18 37 56.5	-0.07	G
				63	6-21	2013-08-10	21 53 39.0	13 52 29.5	-4.83	G
				66	6-33	2013-08-31	04 07 46.0	21 26 29.1	2.74	G
				67	6-12	2013-09-01	17 54 36.0	11 19 31.4	-7.38	G
				68	6-19	2013-09-02	21 10 18.0	14 39 42.1	-4.04	G
Zw 229-015	19 05 25.9	+42 27 40	0.02788	30	6-135	2018-08-31	05 52 11.5	23 10 18.7	4.08	V
				39	6-132	2018-09-08	00 39 51.5	18 28 39.9	-0.61	V
PGC 090334	19 37 33.0	-06 13 05	0.01031	18	6-79	2013-03-10	15 31 13.0	21 25 48.0	1.80	G
NGC 6814	19 42 40.6	-10 19 25	0.00521	40	6-55	2018-09-08	04 43 35.5	22 33 03.9	2.84	V
				21	6-11	2013-03-18	14 15 20.0	20 41 14.9	1.06	G
PG 2130+099	21 32 27.8	+10 08 19	0.06298	15	6-87	2013-03-03	15 52 47.0	21 19 49.6	-0.21	G
				16	6-35	2013-03-04	13 55 03.0	19 25 42.8	-2.11	G
				19	6-113	2013-03-11	13 51 23.0	19 49 38.1	-1.71	G
				58	6-37	2013-07-22	04 20 43.0	19 01 46.0	-2.51	G
NGC 7469	23 03 15.6	+08 52 26	0.01632	28	105-204	2013-04-04	13 51 10.0	21 24 02.3	-1.65	G

**Note.** — Columns (1-3): Galaxy names in increasing right ascension. Column (4): Listed redshift value from literature. Column (5): Session number of observation during observing block. Column (6): Scan number range of a given observation session. Column (7): Date. Columns (8-10): Universal time, local standard time, and hour angle values at the midpoint of the observation on each date. Column (11): Backend of instrument used for observation, G denotes GBT Spectrometer, V denotes VEGAS.

**Table 2**  
Spectral Characteristics

Target	Exp Time (s)	S/N	RMS (K)	Final Resolution (km s <sup>-1</sup> chan <sup>-1</sup> )	Backend
(1)	(2)	(3)	(4)	(5)	(6)
Mrk 1044	14720.6	15.7	0.0021	1.1	V
Ark 120	12684.7	9.8	0.0015	2.4	V
MCG+08-11-011	14405.1	23.4	0.0026	0.8	V
Mrk 6	12904.6	8.2	0.0014	3.0	G
Mrk 374	14163.8	4.7	0.0008	8.8	V
Mrk 79	1261.4	10.4	0.0038	3.0	G
NGC 2617	14843.2	45.4	0.0036	0.3	V
Mrk 704	20883.8	6.5	0.0009	3.2	V
Mrk 110	14160.4	8.9	0.0014	3.2	V
NGC 3227	458.6	13.1	0.0062	3.0	G
NGC 3516	56214.1	8.8	0.0006	4.0	V
SBS1116+583A	12445.8	4.0	0.0009	6.0	G
NGC 3783	4013.1	28.5	0.0059	0.6	G
Mrk 1310	7282.3	8.1	0.0017	3.0	G
NGC 4051	14965.0	112.0	0.0024	0.6	G
NGC 4151	344.1	42.0	0.0151	0.6	G
Mrk 766	15252.1	5.1	0.0008	6.0	G
NGC 4593	10204.7	19.1	0.0031	0.6	G
NGC 4748	14160.5	8.9	0.0013	1.8	G
MCG-06-30-015	12096.8	3.4	0.0015	3.0	G
Mrk 279	14739.9	8.4	0.0013	3.0	G
NGC 5548	13415.8	10.0	0.0011	4.8	G
Mrk 817	13879.6	5.8	0.0007	7.2	G
Mrk 478	13437.6	3.4	0.0012	5.6	V
NGC 5940	13917.5	10.2	0.0020	1.3	V
Mrk 290	11126.6	5.4	0.0009	6.0	G
Mrk 493	13051.6	38.9	0.0024	0.8	V
Zw 229-015	12750.2	6.8	0.0009	6.4	V
1H1934-063	4586.8	11.5	0.0027	1.8	G
NGC 6814	2812.5	81.0	0.0080	0.5	V
NGC 7469	4243.3	4.9	0.0022	3.0	G

**Note.** — Column (2) lists the total time spent on source after removal of contaminated scans. Column (3) lists approximate S/N, and the values were calculated as either a) the average value of the peak fluxes of the horns and mid-profile peak fluxes divided by the RMS of the noise or b) the peak value of the Gaussian-shaped profile divided by the RMS of the noise. Column (4) lists values for the root mean square of the noise in each spectra. Column (5) denotes the final velocity resolution per channel after spectral smoothing was applied (other than initial Hanning smoothing). Column (6) lists the backend of instrument used for observation, G denotes GBT Spectrometer, V denotes VEGAS. The default velocity resolutions of the GBT Spectrometer and VEGAS are 0.3 and 0.08 km s<sup>-1</sup> channel<sup>-1</sup>, respectively.

**Table 3**  
HI Spectroscopic Measurements

Target	$T_L$ gmeasure (K km s <sup>-1</sup> )	$T_L$ BUSYFIT (K km s <sup>-1</sup> )	$W_{50}$ gmeasure (km s <sup>-1</sup> )	$W_{50}$ BUSYFIT (km s <sup>-1</sup> )	$W_{20}$ gmeasure (km s <sup>-1</sup> )	$W_{20}$ BUSYFIT (km s <sup>-1</sup> )	$V_R$ gmeasure (km s <sup>-1</sup> )	$V_R$ BUSYFIT (km s <sup>-1</sup> )	Backend
Mrk 1044	4.95 <sup>+0.06</sup> <sub>-0.03</sub>	5.01 ± 0.05	183.2 <sup>+4.6</sup> <sub>-2.9</sub>	172.2 ± 5.2	196.2 <sup>+4.3</sup> <sub>-10.4</sub>	202.9 ± 3.0	4910.77 <sup>+0.69</sup> <sub>-1.35</sub>	4912.00 ± 0.90	V
Ark 120	3.43 <sup>+0.15</sup> <sub>-0.11</sub>	3.63 ± 0.76	337.3 <sup>+17.0</sup> <sub>-13.1</sub>	315.9 ± 20.8	344.4 <sup>+18.4</sup> <sub>-17.9</sub>	372.6 ± 10.3	9806.38 <sup>+9.22</sup> <sub>-4.51</sub>	9826.00 ± 26.96	V
MCG+08-11-011	14.71 <sup>+0.32</sup> <sub>-0.19</sub>	14.92 ± 1.93	310.8 <sup>+6.7</sup> <sub>-5.1</sub>	293.0 ± 4.6	327.3 <sup>+12.6</sup> <sub>-9.7</sub>	322.4 ± 3.9	6133.26 <sup>+1.31</sup> <sub>-1.64</sub>	6141.00 ± 4.01	V
Mrk 6	3.04 <sup>+0.19</sup> <sub>-0.19</sub>	3.18 ± 0.57	435.8 <sup>+6.4</sup> <sub>-0.5</sub>	440.3 ± 2.8	447.7 <sup>+9.7</sup> <sub>-12.9</sub>	463.7 ± 3.4	5631.35 <sup>+0.48</sup> <sub>-2.98</sub>	5621.00 ± 5.12	G
Mrk 374	0.59 <sup>+0.02</sup> <sub>-0.33</sub>	0.57 ± 0.27	263.8 <sup>+0.9</sup> <sub>-1.0</sub>	252.3 ± 59.9	276.3 <sup>+6.6</sup> <sub>-0.9</sub>	272.8 ± 31.1	13250.00 <sup>+0.07</sup> <sub>-0.06</sub>	13240.00 ± 15.18	V
Mrk 79	5.02 <sup>+0.34</sup> <sub>-0.31</sub>	5.51 ± 0.85	154.4 <sup>+9.7</sup> <sub>-4.5</sub>	159.6 ± 4.2	160.3 <sup>+12.9</sup> <sub>-14.3</sub>	182.8 ± 3.5	6657.41 <sup>+4.76</sup> <sub>-3.88</sub>	6656.00 ± 2.82	G
NGC 2617	18.27 <sup>+0.65</sup> <sub>-0.31</sub>	18.51 ± 0.58	126.3 <sup>+5.9</sup> <sub>-4.2</sub>	111.6 ± 0.5	143.8 <sup>+12.1</sup> <sub>-9.7</sub>	134.9 ± 0.5	4265.06 <sup>+0.63</sup> <sub>-0.28</sub>	4269.00 ± 0.33	V
Mrk 704	0.19 <sup>+0.02</sup> <sub>-0.02</sub>	0.23 ± 0.05	46.9 <sup>+6.6</sup> <sub>-3.2</sub>	52.2 ± 14.2	57.8 <sup>+12.8</sup> <sub>-12.9</sub>	77.1 ± 21.1	9525.87 <sup>+1.60</sup> <sub>-2.55</sub>	9530.00 ± 9.03	V
Mrk 110	0.95 <sup>+0.08</sup> <sub>-0.07</sub>	1.14 ± 0.74	127.2 <sup>+16.6</sup> <sub>-19.2</sub>	104.9 ± 8.6	145.0 <sup>+18.8</sup> <sub>-18.5</sub>	171.2 ± 10.6	10558.90 <sup>+6.36</sup> <sub>-9.49</sub>	10570.00 ± 5.83	V
NGC 3227	28.51 <sup>+0.53</sup> <sub>-0.34</sub>	29.13 ± 5.35	430.1 <sup>+10.8</sup> <sub>-2.8</sub>	135.9 ± 117.8	441.2 <sup>+12.9</sup> <sub>-15.4</sub>	436.3 ± 3.8	1144.74 <sup>+4.33</sup> <sub>-0.82</sub>	1192.00 ± 20.21	G
NGC 3516	0.41 <sup>+0.02</sup> <sub>-0.03</sub>	0.46 ± 0.02	143.4 <sup>+3.4</sup> <sub>-2.6</sub>	134.6 ± 7.4	156.5 <sup>+15.4</sup> <sub>-12.5</sub>	183.9 ± 10.0	2627.31 <sup>+3.76</sup> <sub>-7.67</sub>	2635.00 ± 4.25	V
SBS1116+583A	0.38 <sup>+0.03</sup> <sub>-0.02</sub>	0.42 ± 0.19	142.2 <sup>+9.6</sup> <sub>-10.5</sub>	145.1 ± 37.4	148.2 <sup>+12.9</sup> <sub>-17.3</sub>	167.6 ± 18.8	8376.82 <sup>+7.67</sup> <sub>-2.28</sub>	8378.00 ± 10.44	G
NGC 3783	20.08 <sup>+1.14</sup> <sub>-0.48</sub>	20.34 ± 1.90	145.9 <sup>+9.5</sup> <sub>-2.2</sub>	138.0 ± 1.7	155.4 <sup>+12.4</sup> <sub>-9.3</sub>	152.5 ± 1.5	2916.08 <sup>+3.88</sup> <sub>-0.64</sub>	2913.00 ± 0.92	G
Mrk 1310	2.26 <sup>+0.08</sup> <sub>-0.05</sub>	2.30 ± 0.42	243.2 <sup>+8.0</sup> <sub>-7.8</sub>	238.3 ± 2.1	244.8 <sup>+9.7</sup> <sub>-9.0</sub>	250.5 ± 2.6	5837.72 <sup>+5.55</sup> <sub>-2.50</sub>	5838.00 ± 1.27	G
NGC 4051	60.69 <sup>+0.83</sup> <sub>-0.41</sub>	61.37 ± 0.17	247.9 <sup>+2.8</sup> <sub>-1.1</sub>	236.3 ± 0.1	264.5 <sup>+9.3</sup> <sub>-2.9</sub>	264.5 ± 0.1	703.56 <sup>+0.40</sup> <sub>-0.08</sub>	703.40 ± 0.05	G
NGC 4151	72.73 <sup>+1.26</sup> <sub>-0.82</sub>	72.57 ± 1.85	134.1 <sup>+1.7</sup> <sub>-1.7</sub>	120.3 ± 0.5	152.5 <sup>+8.5</sup> <sub>-0.7</sub>	139.6 ± 0.4	998.56 <sup>+0.14</sup> <sub>-0.41</sub>	997.90 ± 0.32	G
Mrk 766	0.37 <sup>+0.02</sup> <sub>-0.01</sub>	0.37 ± 0.23	120.8 <sup>+7.9</sup> <sub>-1.9</sub>	104.2 ± 14.0	138.6 <sup>+10.1</sup> <sub>-0.6</sub>	126.1 ± 13.9	3899.68 <sup>+0.42</sup> <sub>-2.95</sub>	3904.00 ± 2.65	G
NGC 4593	13.10 <sup>+0.49</sup> <sub>-0.17</sub>	13.20 ± 1.07	361.5 <sup>+11.7</sup> <sub>-3.3</sub>	357.2 ± 1.8	367.0 <sup>+12.7</sup> <sub>-13.6</sub>	367.6 ± 1.6	2501.80 <sup>+1.14</sup> <sub>-5.46</sub>	2501.00 ± 1.57	G
NGC 4748	2.61 <sup>+0.09</sup> <sub>-0.05</sub>	2.68 ± 0.33	315.4 <sup>+9.4</sup> <sub>-2.0</sub>	306.9 ± 5.6	323.3 <sup>+12.2</sup> <sub>-12.3</sub>	332.2 ± 3.6	4183.19 <sup>+3.60</sup> <sub>-2.75</sub>	4196.00 ± 10.92	G
MCG-06-30-015	0.14 <sup>+0.04</sup> <sub>-0.02</sub>	0.18 ± 0.16	28.3 <sup>+9.0</sup> <sub>-6.5</sub>	18.6 ± 28.3	29.0 <sup>+6.4</sup> <sub>-8.3</sub>	43.1 ± 16.1	2353.53 <sup>+4.15</sup> <sub>-3.56</sub>	2358.00 ± 8.98	G
Mrk 279	0.96 <sup>+0.07</sup> <sub>-0.08</sub>	1.23 ± 0.41	146.1 <sup>+18.1</sup> <sub>-22.7</sub>	142.7 ± 12.0	154.6 <sup>+19.3</sup> <sub>-19.3</sub>	219.5 ± 16.2	9211.71 <sup>+8.29</sup> <sub>-6.49</sub>	9210.00 ± 4.94	G
NGC 5548	1.77 <sup>+0.07</sup> <sub>-0.03</sub>	2.03 ± 0.93	189.1 <sup>+10.3</sup> <sub>-6.8</sub>	197.5 ± 15.7	197.3 <sup>+11.8</sup> <sub>-14.0</sub>	251.2 ± 9.3	5145.78 <sup>+5.15</sup> <sub>-1.50</sub>	5159.00 ± 3.79	G
Mrk 817	0.63 <sup>+0.03</sup> <sub>-0.02</sub>	0.67 ± 0.09	293.5 <sup>+7.8</sup> <sub>-7.8</sub>	299.1 ± 54.5	303.7 <sup>+10.0</sup> <sub>-7.8</sub>	331.0 ± 17.7	9420.14 <sup>+4.08</sup> <sub>-3.91</sub>	9438.00 ± 14.24	G
Mrk 478	0.64 <sup>+0.05</sup> <sub>-0.01</sub>	0.67 ± 0.27	294.5 <sup>+11.1</sup> <sub>-10.6</sub>	296.8 ± 65.6	296.9 <sup>+13.6</sup> <sub>-12.3</sub>	327.0 ± 53.7	23879.90 <sup>+5.54</sup> <sub>-5.26</sub>	23870.00 ± 24.61	V
NGC 5940	3.31 <sup>+0.04</sup> <sub>-0.02</sub>	3.30 ± 0.33	188.8 <sup>+0.7</sup> <sub>-0.5</sub>	183.7 ± 1.9	204.5 <sup>+5.9</sup> <sub>-6.5</sub>	201.8 ± 1.9	10209.40 <sup>+0.06</sup> <sub>-0.08</sub>	10210.00 ± 0.65	V
Mrk 290	0.70 <sup>+0.02</sup> <sub>-0.03</sub>	0.73 ± 0.04	192.9 <sup>+12.8</sup> <sub>-3.0</sub>	194.3 ± 8.3	219.0 <sup>+12.9</sup> <sub>-11.1</sub>	224.9 ± 7.4	9087.17 <sup>+1.33</sup> <sub>-6.42</sub>	9091.00 ± 15.51	G
Mrk 493	3.25 <sup>+0.16</sup> <sub>-0.10</sub>	3.20 ± 0.13	54.6 <sup>+6.5</sup> <sub>-8.4</sub>	35.0 ± 10.5	74.7 <sup>+12.1</sup> <sub>-10.9</sub>	55.0 ± 23.7	9442.21 <sup>+1.92</sup> <sub>-0.31</sub>	9442.00 ± 3.85	V
Zw 229-015	0.85 <sup>+0.05</sup> <sub>-0.04</sub>	0.92 ± 0.09	195.7 <sup>+13.0</sup> <sub>-10.6</sub>	202.8 ± 21.7	203.5 <sup>+16.0</sup> <sub>-15.5</sub>	219.9 ± 33.6	8316.11 <sup>+9.39</sup> <sub>-2.12</sub>	8319.00 ± 13.78	V
1H1934-063	4.39 <sup>+0.08</sup> <sub>-0.04</sub>	4.42 ± 0.45	163.6 <sup>+0.9</sup> <sub>-0.6</sub>	160.3 ± 2.0	186.4 <sup>+8.6</sup> <sub>-7.2</sub>	180.4 ± 1.9	3191.42 <sup>+0.06</sup> <sub>-0.09</sub>	3192.00 ± 1.29	G
NGC 6814	54.24 <sup>+2.12</sup> <sub>-1.15</sub>	54.42 ± 0.16	89.0 <sup>+4.2</sup> <sub>-3.1</sub>	79.2 ± 0.1	105.1 <sup>+11.4</sup> <sub>-8.4</sub>	96.2 ± 0.1	1562.34 <sup>+0.36</sup> <sub>-0.16</sub>	1561.00 ± 0.04	V
NGC 7469	1.91 <sup>+0.31</sup> <sub>-0.31</sub>	1.95 ± 0.59	192.6 <sup>+9.8</sup> <sub>-13.9</sub>	184.6 ± 34.0	196.2 <sup>+12.7</sup> <sub>-16.1</sub>	208.8 ± 16.9	4927.87 <sup>+4.99</sup> <sub>-6.79</sub>	4939.00 ± 8.38	G

**Note.** — Spectroscopic measurements from gmeasure and BUSYFIT. Asymmetric error bars for the gmeasure measurements are the result of our bootstrap method discussed in Sec. 2.3. The last column lists the backend used for observation, G denotes GBT Spectrometer, V denotes VEGAS.

**Table 4**  
Previous Measurements

Target	Flux (Jy km s <sup>-1</sup> ) <sup>a</sup> or (K km s <sup>-1</sup> ) <sup>b</sup>	W <sub>50</sub> (km s <sup>-1</sup> )	W <sub>20</sub> (km s <sup>-1</sup> )	V <sub>R</sub> (km s <sup>-1</sup> )	S/N	Ref
Mrk 1044	...	...	489	4932	...	1
	2.58 ± 0.16 <sup>[a]</sup>	193.9	...	4914	...	2
Ark 120	1.51 ± 0.71 <sup>[a]</sup>	194 ± 33	233 ± 50	9807 ± 17	3.8	3
	1.51 <sup>[a]</sup>	97 ± 80	...	9740	2.1	4
	1.965 <sup>[a]</sup>	...	370.3 ± 6.8	9809.2 ± 3.4	...	5
MCG+08-11-011	...	...	...	6146	...	1
	9.53 <sup>[a]</sup>	310 ± 15	...	6133	8.5	6
Mrk 374	8.54 ± 1.94 <sup>[a]</sup>	74 ± 16	121 ± 24	...	6.9	7
Mrk 79	3.94 <sup>[a]</sup>	169 ± 15	...	6657	8.5	6
	3.95 ± 0.46 <sup>[a]</sup>	155 ± 7	...	6659 ± 5	12.1	6
NGC 2617	...	115.1	138.0	4208 ± 8	...	8
	7.02 <sup>[a]</sup>	120 ± 100	...	4267	10.1	9
	9.3 <sup>[a]</sup>	112.4	143.0	4265.2	...	10
	9.3 <sup>[a]</sup>	112.4	...	4264.0	...	11
Mrk 704	0.2 <sup>[a]</sup>	...	250	9510	...	12
NGC 3227	15.495 <sup>[a]</sup>	...	453.4 ± 6.8	1135.6 ± 3.4	...	5
	13.1 <sup>[a]</sup>	430	...	1050 ± 20	...	13
	...	103	437	1146 ± 5	...	14
	10.5 <sup>[b]</sup>	...	234 <sup>[c]</sup>	1284 ± 9	...	15
	14 <sup>[a]</sup>	...	...	1148	...	16
	...	...	...	1152 ± 25	...	17
	...	...	526	1146	...	1
	...	...	293 ± 442	1183	...	18
NGC 3783	8.45 <sup>[a]</sup>	145 ± 5	151 ± 30	2889	15.50	6
	...	145	159	2901 ± 20	...	6
	8.83 <sup>[a]</sup>	147 ± 13	...	...	10.2	9
	...	...	154 ± 7	2917	...	19
NGC 4051	39.8 <sup>[b]</sup>	...	268 <sup>[c]</sup>	706 ± 9	...	15
	30.82 <sup>[a]</sup>	246 ± 8	...	704	46.5	4
	...	...	267 ± 8	704 ± 7	...	20
NGC 4151	46.0 <sup>[b]</sup>	...	156 <sup>[c]</sup>	999 ± 9	...	15
	...	...	142 ± 6	996	...	21
NGC 4593	11.1 ± 1 <sup>[a]</sup>	358 ± 10	378 ± 14	2499 ± 5	...	22
	7.55 ± 0.36 <sup>[a]</sup>	355.5	...	2531	...	2
NGC 5548	1.384 <sup>[a]</sup>	...	321.1 ± 6.8	5169.8 ± 3.4	...	5
	...	110	...	5200 ± 20	...	13
	...	...	472	5142	...	1
	...	218 ± 25	...	5152	4.1	23
	1.73 ± 0.1 <sup>[a]</sup>	303 ± 15	...	5093	9.6	24
Mrk 478	0.48 ± 0.07 <sup>[a]</sup>	395 ± 26	477 ± 39	23406 ± 13	4.81	25
NGC 5940	1.828 <sup>[a]</sup>	187	240	10210 ± 3	9.3	26
	...	...	215	10205	...	1
	1.729 <sup>[a]</sup>	181.4	199.1	10211	11.6	27
	1.80 ± 0.08 <sup>[a]</sup>	189 ± 3	...	10207	12.2	28
	1.36 <sup>[a]</sup>	183 ± 19	...	10214	3.4	6
	...	...	...	10203 ± 32	...	8
Mrk 493	...	...	60	9442	...	1
	1.61 <sup>[a]</sup>	67	...	9430	...	29
	1.398 <sup>[a]</sup>	35.7	59.8	9443	10.4	27
1H1934-063	...	...	...	3070 ± 7	...	8
NGC 6814	29.5 <sup>[a]</sup>	...	94	1565 ± 8	...	30
	...	...	134	1561	...	1
	37.3 ± 4.0 <sup>[a]</sup>	82	105	1563 ± 2	...	31
	33.68 <sup>[a]</sup>	86 ± 8	...	1563	40.2	6
	...	...	124 ± 5	1562 ± 5	...	18
NGC 7469	1.85 ± 0.2 <sup>[a]</sup>	306	...	4877	15.8	6
	3.741 <sup>[a]</sup>	...	525.1 ± 6.8	4899.5 ± 3.4	...	5
	...	570	...	5200 ± 20	...	13
	1.90 <sup>[a]</sup>	358 ± 100	...	4860	3.8	4
	...	515	583	4971 ± 41	...	32
	...	...	395	4916	...	1

**Note.** — References are as follows: 1. Mirabel & Wilson (1984), 2. König et al. (2009), 3. Theureau et al. (2005), 4. Tully et al. (2009b), 5. Ho et al. (2008a), 6. Springob et al. (2005), 7. Davoust & Contini (2004), 8. Patrel et al. (2003), 9. Theureau et al. (2006), 10. Meyer et al. (2004), 11. Doyle et al. (2005), 12. Hutchings (1989), 13. Biermann et al. (1979), 14. van Driel et al. (2001), 15. Dickel & Rood (1978), 16. Davis & Seaquist (1983), 17. Peterson (1979), 18. Huchtmeier & Richter (1989), 19. Theureau et al. (1998), 20. Fisher & Tully (1981), 21. Tift & Cocke (1988), 22. Staveley-Smith & Davies (1987), 23. Stierwalt et al. (2005), 24. Haynes et al. (2013), 25. Teng et al. (2013), 26. Lewis (1983), 27. Lewis (1987), 28. Haynes et al. (2011), 29. Haynes & Giovanelli (1984), 30. Shostak (1978), 31. Koribalski et al. (2004) 32. Richter & Huchtmeier (1982).

<sup>a</sup>Flux measured in Jy km s<sup>-1</sup>.

<sup>b</sup>Flux measured in K km s<sup>-1</sup>.

<sup>c</sup>Width corrected for resolution of instrument, and defined as half-width at one-quarter peak intensity. Displayed as double the original value.

**Table 5**  
z Comparisons

Target	z (HI) This Work	z (HI) Lit	Ref	z (Opt) Lit	z (IR) Lit	z (UV) Lit	Ref
(1)	(2)	(3)	(4)	(5)	(6)	(7)	(8)
Mrk 1044	0.01638	...	...	0.01621	...	0.01600	10,11
Ark 120	0.03271	0.03271	1	0.03312	...	...	12
MCG+08-11-011	0.02046	0.02046	2	0.02064	...	...	12
Mrk 6	0.01878	0.01881	3	0.01701 - 0.01975	...	...	13
Mrk 374	0.04420	0.04263	4	0.04385	...	...	14
Mrk 79	0.02221	0.02221	2	0.02192 - 0.02242	0.02220	...	13,15
NGC 2617	0.01423	0.01421	5	0.01432	...	...	13
Mrk 704	0.03177	...	...	0.02923 - 0.02991	0.02900	0.02900	16,12,15,11
Mrk 110	0.03522	...	...	0.03529	...	...	17
NGC 3227	0.00382	...	...	0.00371 - 0.00383	0.00400	...	18,19,15
NGC 3516	0.00876	...	...	0.00872 - 0.00884	0.00900	...	18,17,15
SBS1116+583A	0.02794	...	...	0.02788	...	...	20
NGC 3783	0.00973	0.00973	6	0.00851 - 0.01022	0.00970	...	13,15
Mrk 1310	0.01947	...	...	0.01956 - 0.02000	...	...	21,22
NGC 4051	0.00235	0.00234	7	0.00209 - 0.00235	0.00200	...	18,19,15
NGC 4151	0.00333	0.00333	8	0.00319 - 0.00320	0.00300	...	23,18,15
Mrk 766	0.01301	...	...	0.01293 - 0.01300	0.01293 - 0.01300	...	24,22,25,15
NGC 4593	0.00835	...	...	0.00797 - 0.00900	0.00900	...	13,26
NGC 4748	0.01395	...	...	0.01463	0.01500	...	27,15
MCG-06-30-015	0.00785	...	...	0.00775	0.00775 - 0.00800	...	28,29,15
Mrk 279	0.03073	...	...	0.02970	0.03025 - 0.03045	0.03050	30,31,32,33
NGC 5548	0.01716	0.01699 - 0.01727	3	0.01645 - 0.01651	0.01700 - 0.01717	0.01720	34,35,20,15,31,33
Mrk 817	0.03142	...	...	0.03120	0.03100 - 0.03146	0.03130	30,15,32,33
Mrk 478	0.07965	...	...	0.07500 - 0.07906	0.07700	0.07700	36,12,37,11
NGC 5940	0.03405	0.03408	2	0.03369 - 0.03400	...	0.03400	38,39,11
Mrk 290	0.03031	...	...	0.03023 - 0.03040	0.03000 - 0.03062	0.02960	40,20,37,31,33
Mrk 493	0.03150	...	...	0.03131 - 0.03133	...	0.03100	12,16,11
Zw 229-015	0.02774	...	...	0.02660 - 0.02788	...	...	41,42
1H1934-063	0.01065	0.01025	5	0.01060	0.01059	...	43,26
NGC 6814	0.00521	0.00521 - 0.00522	9,2	0.00479 - 0.00503	0.00567	...	18,12,44
NGC 7469	0.01644	0.01627	3	0.01580 - 0.02000	0.01600	...	45,16,15

**Note.** — The uncertainties on the redshift measurements ranged from  $\sim 0.002\%$ – $0.15\%$ . Column (4) denotes the references for  $z$  from HI analysis and are as follows: 1. Theureau et al. (2005), 2. Springob et al. (2005), 3. Gallimore et al. (1999), 4. Davoust & Contini (2004), 5. Paturel et al. (2003), 6. Theureau et al. (1998), 7. Verheijen & Sancisi (2001), 8. Wolfinger et al. (2013), 9. Koribalski et al. (2004). Column (8) denotes the references for all other  $z$  values and are as follows: 10. Huchra et al. (1993), 11. Monroe et al. (2016), 12. de Vaucouleurs et al. (1991), 13. NED, 14. Rines et al. (2000), 15. Hernán Caballero (2012), 16. Falco et al. (1999), 17. Keel (1996), 18. Humason et al. (1956), 19. Hakobyan et al. (2012), 20. Oh et al. (2015), 21. Ho & Kim (2009), 22. Stocke et al. (1991), 23. Wong et al. (2008), 24. Ramella et al. (1995), 25. Smith et al. (1987), 26. Strauss et al. (1992), 27. Maza & Ruiz (1989), 28. Kaldare et al. (2003), 29. Fisher et al. (1995), 30. Osterbrock & Pogge (1987), 31. Mendoza-Castrejón et al. (2015), 32. Strauss & Huchra (1988), 33. Tilton et al. (2012), 34. Haynes et al. (2011), 35. Humason et al. (1956), 36. Richards et al. (2009), 37. Shi et al. (2014), 38. Rines et al. (2016), 39. Wu & Jia (2010), 40. Argudo-Fernández et al. (2015), 41. Smith et al. (2015), 42. Proust et al. (1995), 43. Panessa et al. (2011), 44. Riffel et al. (2013), 45. Joshi et al. (2012).

**Table 6**  
Mass Estimates

Target	Morphology	$D_L$ (Mpc)	Ref	$\text{Log } M_{\text{BH}}$ ( $M_\odot$ )	Ref	$\text{Log } M_{\text{STARS}}$ ( $M_\odot$ )	$\text{Log } M_{\text{GAS}}$ ( $M_\odot$ )	$\text{Log } M_{\text{BARY}}$ ( $M_\odot$ )
(1)	(2)	(3)	(4)	(5)	(6)	(7)	(8)	(9)
Mrk 1044	SB(s)c <sup>b</sup>	69.1 ± 7.0	1	6.71 <sup>+0.12</sup> <sub>-0.10</sub>	7	9.88 ± 0.51	9.60 <sup>+0.08</sup> <sub>-0.08</sub>	10.06 ± 0.39
Ark 120	Sb pec <sup>a</sup>	139.6 ± 7.1	2	8.07 <sup>+0.35</sup> <sub>-0.06</sub>	8	11.04 ± 0.23	10.05 <sup>+0.05</sup> <sub>-0.04</sub>	11.08 ± 0.21
MCG+08-11-011	SBc <sup>b</sup>	86.5 ± 7.0	1	7.43 <sup>+0.15</sup> <sub>-0.15</sub>	9	11.37 ± 0.50	10.27 <sup>+0.07</sup> <sub>-0.07</sub>	11.40 ± 0.48
Mrk 6	Sb <sup>b</sup>	80.6 ± 7.1	2	8.10 <sup>+0.04</sup> <sub>-0.04</sub>	8	10.68 ± 0.23	9.52 <sup>+0.07</sup> <sub>-0.03</sub>	10.71 ± 0.22
Mrk 374	SBc <sup>b</sup>	190.2 ± 7.2	1	7.30 <sup>+0.31</sup> <sub>-0.31</sub>	9	10.85 ± 0.50	9.55 <sup>+0.07</sup> <sub>-0.03</sub>	10.87 ± 0.49
Mrk 79	SBb <sup>a</sup>	94.0 ± 7.2	2	7.61 <sup>+0.11</sup> <sub>-0.14</sub>	8	10.69 ± 0.23	9.87 <sup>+0.07</sup> <sub>-0.07</sub>	10.75 ± 0.21
NGC 2617	Sc <sup>b</sup>	59.9 ± 7.0	1	7.49 <sup>+0.14</sup> <sub>-0.14</sub>	9	10.47 ± 0.51	10.04 <sup>+0.09</sup> <sub>-0.09</sub>	10.61 ± 0.42
Mrk 704	SBab <sup>b</sup>	135.5 ± 7.1	1	7.61 <sup>+0.06</sup> <sub>-0.06</sub>	10	11.10 ± 0.40	8.77 <sup>+0.06</sup> <sub>-0.06</sub>	11.10 ± 0.40
Mrk 110	Sc <sup>b</sup>	150.9 ± 7.1	2	7.29 <sup>+0.10</sup> <sub>-0.10</sub>	8	10.69 ± 0.23	9.56 <sup>+0.05</sup> <sub>-0.05</sub>	10.72 ± 0.22
NGC 3227	SAB(s) pec <sup>a</sup>	16.1 ± 2.4	3	6.78 <sup>+0.08</sup> <sub>-0.11</sub>	8	11.03 ± 0.23	9.09 <sup>+0.11</sup> <sub>-0.11</sub>	11.04 ± 0.23
NGC 3516	(R)SB(s) <sup>a</sup>	37.1 ± 7.0	2	7.40 <sup>+0.04</sup> <sub>-0.06</sub>	8	10.52 ± 0.25	7.97 <sup>+0.14</sup> <sub>-0.14</sub>	10.52 ± 0.25
SBS1116+583A	SBc <sup>b</sup>	118.5 ± 7.1	2	6.56 <sup>+0.08</sup> <sub>-0.08</sub>	8	10.38 ± 0.23	8.96 <sup>+0.06</sup> <sub>-0.06</sub>	10.40 ± 0.22
NGC 3783	(R')SB(r)a <sup>a</sup>	25.1 ± 5.0	4	7.37 <sup>+0.08</sup> <sub>-0.08</sub>	8	10.48 ± 0.24	9.33 <sup>+0.15</sup> <sub>-0.15</sub>	10.51 ± 0.23
Mrk 1310	Sbc <sup>b</sup>	82.7 ± 7.0	2	6.21 <sup>+0.07</sup> <sub>-0.09</sub>	8	9.98 ± 0.23	9.41 <sup>+0.07</sup> <sub>-0.07</sub>	10.08 ± 0.19
NGC 4051	SAB(rs)bc <sup>a</sup>	9.8 ± 3.4	4	6.13 <sup>+0.12</sup> <sub>-0.16</sub>	8	10.13 ± 0.25	8.99 <sup>+0.23</sup> <sub>-0.23</sub>	10.16 ± 0.24
NGC 4151	(R')SAB(rs)ab <sup>a</sup>	13.9 ± 3.3	4	7.56 <sup>+0.05</sup> <sub>-0.05</sub>	8	10.40 ± 0.25	9.37 <sup>+0.17</sup> <sub>-0.17</sub>	10.44 ± 0.23
Mrk 766	SBc <sup>b</sup>	54.4 ± 7.0	2	6.82 <sup>+0.05</sup> <sub>-0.06</sub>	8	10.18 ± 0.24	8.27 <sup>+0.10</sup> <sub>-0.10</sub>	10.19 ± 0.24
NGC 4395	SA(s)m <sup>a</sup>	4.1 ± 0.4	5	5.45 <sup>+0.13</sup> <sub>-0.15</sub>	8	9.08 ± 0.41	9.21 <sup>+0.08</sup> <sub>-0.08</sub>	9.45 ± 0.23
NGC 4593	(R)SB(rs)b <sup>a</sup>	37.7 ± 7.5	4	6.88 <sup>+0.08</sup> <sub>-0.10</sub>	8	10.83 ± 0.25	9.50 <sup>+0.15</sup> <sub>-0.15</sub>	10.85 ± 0.24
NGC 4748	Sab <sup>b</sup>	61.6 ± 7.0	2	6.41 <sup>+0.11</sup> <sub>-0.18</sub>	8	10.46 ± 0.24	9.22 <sup>+0.09</sup> <sub>-0.09</sub>	10.48 ± 0.23
MCG-06-30-015	SO <sup>b</sup>	25.5 ± 3.5	4	6.20 <sup>+0.35</sup> <sub>-0.35</sub>	8	10.02 ± 0.22	7.17 <sup>+0.12</sup> <sub>-0.12</sub>	10.02 ± 0.22
Mrk 279	SO <sup>a</sup>	129.7 ± 7.1	2	7.44 <sup>+0.10</sup> <sub>-0.13</sub>	8	11.07 ± 0.23	9.43 <sup>+0.05</sup> <sub>-0.05</sub>	11.08 ± 0.23
NGC 5548	(R')SA(s)0/a <sup>a</sup>	75.0 ± 7.3	6	7.72 <sup>+0.02</sup> <sub>-0.02</sub>	8	11.10 ± 0.23	9.22 <sup>+0.08</sup> <sub>-0.08</sub>	11.11 ± 0.23
Mrk 817	SBc <sup>a</sup>	134.2 ± 7.1	2	7.59 <sup>+0.02</sup> <sub>-0.07</sub>	8	10.97 ± 0.23	9.28 <sup>+0.08</sup> <sub>-0.04</sub>	10.98 ± 0.23
Mrk 478	Sab <sup>b</sup>	351.6 ± 7.4	1	7.40 <sup>+0.18</sup> <sub>-0.18</sub>	11	11.15 ± 0.50	10.12 <sup>+0.03</sup> <sub>-0.02</sub>	11.19 ± 0.47
NGC 5940	SBc <sup>b</sup>	145.5 ± 7.1	1	7.04 <sup>+0.07</sup> <sub>-0.07</sub>	12	11.06 ± 0.40	10.07 <sup>+0.04</sup> <sub>-0.04</sub>	11.10 ± 0.37
Mrk 290	SO <sup>b</sup>	130.0 ± 7.3	6	7.28 <sup>+0.06</sup> <sub>-0.06</sub>	8	10.52 ± 0.40	9.30 <sup>+0.05</sup> <sub>-0.05</sub>	10.54 ± 0.38
Mrk 493	SB(r)c <sup>b</sup>	134.3 ± 7.1	1	6.41 <sup>+0.04</sup> <sub>-0.09</sub>	7	10.44 ± 0.50	9.99 <sup>+0.05</sup> <sub>-0.05</sub>	10.57 ± 0.41
Zw 229-015	(R)SBc <sup>b</sup>	120.2 ± 7.2	2	6.91 <sup>+0.08</sup> <sub>-0.12</sub>	8	10.32 ± 0.23	9.31 <sup>+0.05</sup> <sub>-0.05</sub>	10.36 ± 0.21
1H1934-063	Sbc <sup>b</sup>	45.2 ± 7.0	1	6.40 <sup>+0.17</sup> <sub>-0.20</sub>	11	10.53 ± 0.21	9.18 <sup>+0.12</sup> <sub>-0.12</sub>	10.55 ± 0.20
NGC 6814	SAB(rs)bc <sup>a</sup>	21.8 ± 7.0	2	7.04 <sup>+0.06</sup> <sub>-0.06</sub>	8	10.34 ± 0.29	9.64 <sup>+0.22</sup> <sub>-0.22</sub>	10.42 ± 0.26
NGC 7469	(R')SAB(rs)a <sup>a</sup>	68.8 ± 7.0	2	6.96 <sup>+0.05</sup> <sub>-0.05</sub>	8	10.88 ± 0.23	9.18 <sup>+0.10</sup> <sub>-0.10</sub>	10.89 ± 0.23

**Note.** — Mass estimates and morphologies for the AGNs in this study. Morphological classifications in column (2) are from NED or the B/T ratios from the results of the surface brightness decomposition parameters from [Bentz et al. \(2009\)](#), [Bentz et al. \(2013\)](#), [Bentz et al. \(2016\)](#), and [Bentz & Manne-Nicholas \(2018\)](#). Classifications were assigned to the B/T values based on Figure 6 of [Kent \(1985\)](#) (see Sec. 4.1). Column (3) lists the distances employed for each galaxy and are described in Sec. 3.1. The references listed in column (4) are for the sources of the distance values and are as follows: 1. estimated from redshift of HI emission line; this work, 2. [Bentz & Manne-Nicholas \(2018\)](#), 3. [Tonry et al. \(2001\)](#), 4. [Courtois et al. \(2009\)](#), 5. [Thim et al. \(2004\)](#), 6. [Bentz et al. \(2013\)](#). Column (5) lists the SMBH values of each galaxy and are discussed in Sec. 3.4. The references listed in column (6) are for the sources of the  $M_{\text{BH}}$  values and are as follows: 7. mass calculated with  $\tau_{H\beta}$  by [Hu et al. \(2015\)](#),  $\sigma_{\text{line}}$  by [Du et al. \(2016\)](#), and scaled with  $\langle f \rangle = 4.3$ , 8. the AGN Black Hole Mass Database ([Bentz & Katz 2015](#)), 9. the virial mass from [Fausnaugh et al. \(2017\)](#) scaled with  $\langle f \rangle = 4.3$ , 10. the virial mass from [De Rosa et al. \(2018\)](#) scaled with  $\langle f \rangle = 4.3$ , 11. preliminary mass estimate from in-hand reverberation mapping data, 12. mass calculated from the  $\sigma_{\text{line}}$  by [Barth et al. \(2015\)](#),  $\tau_{H\beta}$  by [Barth et al. \(2013\)](#), and scaled with  $\langle f \rangle = 4.3$ .  $M_{\text{STARS}}$  estimates are listed in column (7) and the calculations are described in Sec. 3.3. The calculations for  $M_{\text{GAS}}$  estimates listed in column (8) are described in Sec. 3.2.  $M_{\text{BARY}}$  values in column (9) were calculated as  $M_{\text{GAS}} + M_{\text{STARS}}$ .

<sup>a</sup>Classification from NED.

<sup>b</sup>Derived classification from surface brightness decompositions.